
Tilt and Average : Geometric Adjustment of the Last Layer for Recalibration

Gyusang Cho¹ Chan-Hyun Youn¹

Abstract

After the revelation that neural networks tend to produce overconfident predictions, the problem of calibration, which aims to align confidence with accuracy to enhance the reliability of predictions, has gained significant importance. Several solutions based on calibration maps have been proposed to address the problem of recalibrating a trained classifier using additional datasets. In this paper, we offer an algorithm that transforms the weights of the last layer of the classifier, distinct from the calibration-map-based approach. We concentrate on the geometry of the final linear layer, specifically its angular aspect, and adjust the weights of the corresponding layer. We name the method Tilt and Average(TNA), and validate the calibration effect empirically and theoretically. Through this, we demonstrate that our approach, in addition to the existing calibration-map-based techniques, can yield improved calibration performance. Code available : [URL](#).

1. Introduction

As neural networks demonstrate their powerful performance across various fields, their reliability has become a significant concern. The fact that neural networks are miscalibrated(Guo et al., 2017) and are possible to assign high confidence to wrong predictions, is a notable issue in diverse applications, especially in scenarios that are safety-critical(medical usage(Litjens et al., 2017), autonomous-driving(Yurtsever et al., 2020)), or high-stake and cost-effective(satellite(Moskolař et al., 2021)). To resolve this issue, model calibration is studied to reflect reliable confidence estimates to quantify the uncertainty of the prediction.

We target the *recalibration* problem for a model trained on a training set, using an additional dataset. Therefore, the

¹Department of Electrical Engineering, KAIST, Daejeon, Republic of Korea. Correspondence to: Gyusang Cho <cks1463@kaist.ac.kr>.

primary focus is on improving the calibration performance of the model while maintaining accuracy as learned during the original training. The methods introduced in conventional works for recalibration are more focused on fitting a calibration map of the neural network. The calibration map is an additionally designed function that takes the logit of the predicted probability as the input, and outputs calibrated results(Guo et al., 2017; Zhang et al., 2020; Tomani et al., 2022).

In this paper, we adopt a slightly different perspective, opting to modify the weights of the final linear layer rather than creating a new calibration map. Exploiting the neural network as a feature extractor, the last linear layer transforms high-dimensional deep features into class-specific scores for probability estimation. In this process, we propose techniques that leverage the geometry of the feature space where this transformation occurs. As a result, the proposed algorithm, when combined with traditional calibration-map methods, exhibits superior calibration performance compared to conventional approaches.

In summary, we make the following contributions to this work :

- We propose a recalibration algorithm leveraging the geometry of the last linear layer, deviating from the previously suggested calibration-map approach. Due to the **orthogonality** of this method, it can seamlessly integrate with existing techniques for recalibration problems, and achieve **better calibration performance** than using the conventional approach alone.
- We provide theoretical or experimental background based on the geometric interpretation of the feature space and linear layer. We also verify data efficiency and algorithmic integrity through ablation studies.

2. Background & Related Works

2.1. Background

Notation. We consider the classification task with the labeled dataset. Let the input data $X \in \mathcal{X}$ and the corresponding label $Y \in \mathcal{Y}$ denote the data-label pair, with $C := |\mathcal{Y}|$ classes. Let the model $M = (f, h)$ trained on the training split of the data, consists of the feature extractor

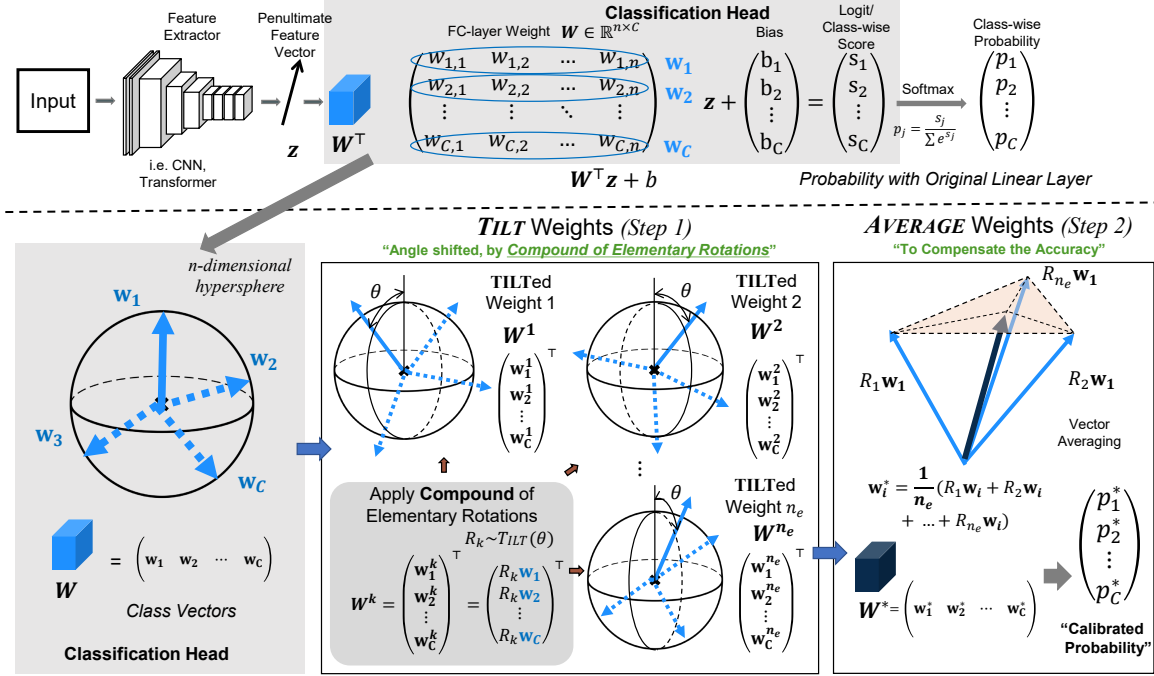


Figure 1. Overview of the proposed algorithm. We take the original weight W of the last linear layer (FC-layer), generate multiple “TILT”ed weights W^1, W^2, \dots, W^{n_e} from the original weight with relaxed confidence, and “AVERAGE” the generated weights to compensate possible accuracy loss. The detailed information can be found in Section 3.1.

$f : \mathcal{X} \rightarrow \mathbb{R}^n$, and the last classifier function $h : \mathbb{R}^n \rightarrow \mathbb{R}^C$. Then the prediction \hat{Y} and the confidence \hat{P} of a single input X can be written with $\hat{Y} = \arg \max_i h(f(X))$, and $\hat{P} = \max_i \sigma(h(f(X)))$ for the class $i \in [C]$, where the σ is a softmax function.

Penultimate Feature, Last Linear Layer, and Confidence.

In common cases, the classifier function is a linear layer (fully connected layer) (Kang et al., 2020). The linear layer applies affine transform on the condensed feature vector $\mathbf{z} = f(X) \in \mathbb{R}^n$ from the feature extractor f , i.e., $h(\mathbf{z}) = \mathbf{W}^T \mathbf{z} + \mathbf{b}$, where $\mathbf{W} = [\mathbf{w}_1 \dots \mathbf{w}_C] \in \mathbb{R}^{n \times C}$ denotes the weight matrix and the bias vector $\mathbf{b} \in \mathbb{R}^C$. We term the vector \mathbf{z} as the *penultimate feature* or *pf*, of which the vector is the output of the penultimate layer of the network. We also designate \mathbf{w}_i , the i th vector of the classifier weight matrix \mathbf{W} , as the i th *class vector*, and the weight matrix *original weight*.

Let the logit vector $\mathbf{s} = h(\mathbf{z})$, then the element of the logit vector for each class can be computed with the dot product representation,

$$s_i = \mathbf{w}_i \cdot \mathbf{z} + b_i = \|\mathbf{w}_i\| \|\mathbf{z}\| \cos \angle(\mathbf{w}_i, \mathbf{z}) + b_i, \forall i \in [C] \quad (1)$$

Recall that $\hat{P} = \max_i \sigma(h(\mathbf{z}))$, the confidence \hat{P} of the sample X with *pf* \mathbf{z} can be written as,

$$\hat{P} = \max_i \frac{\exp(\|\mathbf{w}_i\| \|\mathbf{z}\| \cos \angle(\mathbf{w}_i, \mathbf{z}) + b_i)}{\sum_k \exp(\|\mathbf{w}_k\| \|\mathbf{z}\| \cos \angle(\mathbf{w}_k, \mathbf{z}) + b_k)}, \quad (2)$$

where $\angle(u, v)$ denote the angle between two vectors u, v . Despite the apparent simplicity of the geometric decomposition in Eq. 1, 2, significant insights can be derived from this approach. Two properties: 1) the **norm** (magnitude) of the class vector $\|\mathbf{w}_i\|$, and 2) the **angle** between the class vector and the penultimate feature $\angle(\mathbf{w}_i, \mathbf{z})$, are the important factors for determining the confidence. In this paper, we focus on a method that involves adjusting the **angular property**.

2.2. Related Works

Calibration, Calibration Error. Confidence calibration is a problem to correctly predict the probability estimate (i.e. confidence) for a decision that a system has made. Not only the neural network should make a correct decision, but also it should provide a probability that reflects the ground truth correctness likelihood to make the model interpretable and reliable. As observed in (Guo et al., 2017), neural networks exhibit poor calibration, typically displaying over-confidence in their predictions (Ovadia et al., 2019; Ashukha et al., 2020). Formally, the *perfectly calibrated* classifier can be defined as the classifier that outputs (\hat{Y}, \hat{P}) to be $\mathbb{P}(\hat{Y} = Y | \hat{P} = p) = p, \forall p \in [0, 1]$. Following the definition, we evaluate the misalignment, Calibration Error (CE), $CE = \mathbb{E}_{\hat{P}} [\mathbb{P}(\hat{Y} = Y | \hat{P} = p) - p]$. The classifier with low CE is considered to be more calibrated.

Recalibration, which is also known as post-hoc calibration, supposes that the classifier trained on the training set is given, and aims to adjust a proper scoring rule to the calculated probability of the network with additional calibration dataset. Most of the work seeks to fit an additional function $f_{cal} : \mathbb{R}^C \rightarrow \mathbb{R}^C$ called *calibration map* which transforms the logit vector s to the calibrated probability vector to yield calibrated confidence estimate \hat{P}' . The calibration map f_{cal} is then trained with an additional set of data apart from the training data. Popular approaches to design f_{cal} includes applying Platt scaling (Platt, 1999), temperature scaling (Guo et al., 2017) and its variants (Zhang et al., 2020; Ding et al., 2021; Tomani et al., 2022; Joy et al., 2023), Dirichlet scaling (Kull et al., 2019), isotonic regression (Zadrozny & Elkan, 2002), binning-based approaches (Naeni et al., 2015; Patel et al., 2021), sample ranking (Rahimi et al., 2020; Ma & Blaschko, 2021), non-parametric methods (Wenger et al., 2020), and atypicality-aware map (Yuksekonul et al., 2023).

Orthogonal to the previous findings of designing an advanced calibration map, we take a different perspective and present an algorithm that maps the original weight \mathbf{W} to an alternative weight \mathbf{W}' . Treating the weight matrix as a set of *class vectors* $\{w_i\}_{i=1}^C$ that determine each element of the logit vector, we seek an alternative set of *class vectors* of $\{w'_i\}_{i=1}^C$ that may result in lower calibration error.

3. Method

We aim to design a transformation $Q : \mathbb{R}^n \rightarrow \mathbb{R}^n$, that maps the *class vectors* $\{w_i\}_{i=1}^C$ to alternative *class vectors* $\{w'_i\}_{i=1}^C$ that exhibit better calibrated confidence without compromising accuracy. The proposed approach ‘‘Tilt and Average’’ (TNA) consists of two-fold steps: 1) ‘‘TILT-ing’’ the class vectors using rotation transformation, and 2) AVERAGE-ing weights to supplement the compromised accuracy.

3.1. ‘‘TILT’’ the *class vectors* for angle adjustment.

Rotation transformation is a particular type of unitary linear transformation in n -dimensional Euclidean space. The key characteristic of a rotation transformation is that the transformed vector undergoes a change in direction without altering its norm, or magnitude. Hence, one might infer that applying a rotation transform to the class vector w_i could potentially allow for the adjustment of $\angle(w_i, \mathbf{z})$. Consequently, we elaborate on the algorithm and theoretical background for this purpose as described below.

In this step, we propose an algorithm that can perform rotation transformation to a specified ‘‘intensity’’. Here, the term ‘‘intense’’ transform refers to a transformation that introduces significant changes in the angle, while a rotation transform with minimal changes in the angle is considered to have weak intensity. For example, the identity transformation on

the class vectors can be regarded as having an intensity of 0, as it introduces no change in angle. Therefore, we first define the concept of ‘‘mean Rotation over Classes’’ or mRC, which can be considered as a metric for the intensity.

Definition 3.1. (*mean Rotation over Classes*) Given the original weight \mathbf{W} and a rotation matrix R , the *mean Rotation over Classes* (mRC) is defined as,

$$mRC(\mathbf{W}, R) = \frac{1}{C} \sum_{i=1}^C \arccos \left(\frac{\langle w_i, R w_i \rangle}{\|w_i\| \|R w_i\|} \right) \quad (3)$$

mRC is a metric quantifying, in the context of predetermined weight matrices and rotation matrices, the typical degree to which each class vector is rotated.

3.1.1. GENERATING n -DIMENSIONAL ROTATION MATRIX WITH mRC

The main inspiration is from Euler’s rotation theorem (Euler, 1776) in three-dimensional space that any rotation matrix R can be generated via elementary rotations, $R = R_x(\alpha)R_y(\beta)R_z(\gamma)$, where $R_x(\alpha)$ states the rotation matrix that rotates of angle α around the X-axis, and vice-versa. The elementary rotation in dimension n , is dubbed Givens rotation (Givens, 1958).

We generate a rotation transformation in n -dimensional space with a compound of elementary rotations as in Euler’s theorem. Let n_r denote the number of compound of elementary rotations. The elementary rotation matrix $R_k^e(\theta_{t_k})$ ($k \in [n_r]$) can be readily created by using a random angle $\theta_{t_k} = \tau \times \theta_s$, where $\tau \sim \text{Beta}(\alpha, \beta)$, and θ_s is a pre-established angle given as a hyperparameter. We randomly select 2 indexes $k_1, k_2 \in [n]$ from an n -dimensional identity matrix. Then we flip the elements of columns and rows k_1, k_2 to 2-dimensional rotation matrix, with $r_{k_1 k_1} = \cos \theta_{t_i}, r_{k_1 k_2} = -\sin \theta_{t_i}, r_{k_2 k_1} = \sin \theta_{t_i}, r_{k_2 k_2} = \cos \theta_{t_i}$. We repeat this process n_r times as Eq. 4,

$$R = R_1^e(\theta_{t_1}) R_2^e(\theta_{t_2}) \dots R_{n_r}^e(\theta_{t_{n_r}}), \quad (4)$$

which we term the new weight matrix $\mathbf{W}^{\text{TILT}} = R\mathbf{W}$ as *tilted weight*.

The results of measuring mRC, derived from the rotation matrix R generated by the provided algorithm and the original weight \mathbf{W} , are represented in Fig. 2. For the experiment, we take three benchmark datasets CIFAR10, CIFAR100 (Krizhevsky et al., 2010), ImageNet (Deng et al., 2009), with trained weights on the architecture of WideResNet28x10 (Zagoruyko & Komodakis, 2016), MobileNetV2 (Sandler et al., 2018), and ResNet50 (He et al., 2016a) respectively. We generate 2,000 tilted weights for each dataset. The proposed algorithm can produce a rotation matrix with a specific mRC, demonstrating variations by

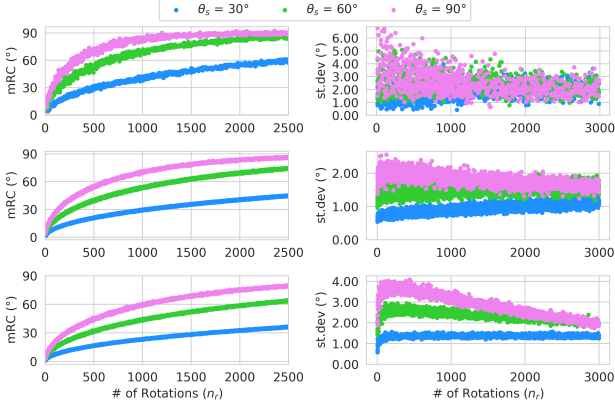


Figure 2. Plots of mRC corresponding to the number of rotations (n_r) with different values of θ_s . Each point corresponds to a single tilted weight. When the number of rotations increases, mRC increases as well. Each row states for different dataset-model pair: CIFAR10-WRN28x10(upper), CIFAR100-MobileNetV2(middle), ImageNet-ResNet50(lower). Across datasets and models, the proposed algorithm can generate a rotation matrix with certain mRC , by changing the number of rotations n_r .

adjusting the number of rotations n_r across datasets and models. Consequently, we design the algorithm as in Alg. 1-TILT. Additionally from the plot, it can be observed that as n_r increases, mRC increases and eventually converges to around 90° . Applying a transformation with high intensity leads to a decreasing correlation with the original vector, aligning with the near-orthogonal theorem (Blum et al., 2020), which states that, with high probability, high-dimensional arbitrary vectors become orthogonal. (Also see Section 5)

3.1.2. VALIDATING TILT

In this section, we theoretically demonstrate that the tilted weight generated by the algorithm presented above allows for the adjustment of angles between class vectors and penultimate features. Additionally, we illustrate the statistical properties associated with this adjustment. With some additional assumptions, we theoretically show the relaxing effect on confidence. Finally, we experimentally confirm that the tilted weight transformed by the algorithm TILT, indeed has an effect on adjusting angles.

With rotation matrix R , we first define the difference after rotation $\Delta_{\mathbf{z},i} := \angle(R\mathbf{w}_i, \mathbf{z}) - \angle(\mathbf{w}_i, \mathbf{z})$, where \mathbf{z} denote the pf.

Theorem 3.2. (Class-wise Effect of TILT.) *Let there be an original weight \mathbf{W} , and rotation matrix R . Also, let ψ_i to be $\angle(\mathbf{w}_i, \mathbf{z})$. Suppose the rotation matrix R rotates the i -th class vector with θ , $\angle(\mathbf{w}_i, R\mathbf{w}_i) = \theta$. We further*

assume that inequality $0^\circ < \theta < \psi_i < 90^\circ$ holds for penultimate feature \mathbf{z} . Lastly, we assume equal probability on the possible rotations of R . That is, let V be the set of vectors rotated from a vector u by all possible rotation matrices R , that rotates with angle θ , then for $\forall v_1, v_2 \in V$, $\mathbb{P}(Ru = v_1) = \mathbb{P}(Ru = v_2)$. Let \mathbb{M} be the mode of $\Delta_{\mathbf{z},i}$. Then the equation below holds,

$$\mathbb{M}[\Delta_{\mathbf{z},i}] = \arccos(\cos \psi_i \cos \theta) - \psi_i. \quad (5)$$

We provide the proof of Thm. 3.2 in the appendix, Sec. C. Building upon the insights derived from the given Thm 3.2, with additional assumptions, one can observe a confidence relaxation effect akin to the proposition as Prop. 3.3.

Proposition 3.3. (Confidence Relaxation.) *For an input sample X and the corresponding penultimate feature \mathbf{z} , we assume that the equalities below hold across all the classes in addition to the assumptions made in Thm. 3.2, $\forall i \in [C]$, $\angle(\mathbf{w}_i, R\mathbf{w}_i) = \theta$ and $\Delta_{\mathbf{z},i} = \arccos(\cos \psi_i \cos \theta) - \psi_i$, and element of bias vector be $b_{k_1} = b_{k_2}$, $\forall k_1, k_2 \in [C]$. Then the tilted weight $\mathbf{W}' = R\mathbf{W}$ has a smaller confidence estimate for sample x .*

Proof. Let \hat{P}_X be the confidence estimate of sample X from original weight \mathbf{W} , and \hat{P}'_X be the confidence estimate of sample x on the tilted weight \mathbf{W}' . When applying the assumed conditions to Eq. 2, then \hat{P}_X and \hat{P}'_X can be written as,

$$\hat{P}_X = \max_i \frac{\exp(\|\mathbf{w}_i\| \|\mathbf{z}\| \cos \psi_i)}{\sum_k \exp(\|\mathbf{w}_k\| \|\mathbf{z}\| \cos \psi_k)}, \quad (6)$$

$$\hat{P}'_X = \max_i \frac{\exp(\|\mathbf{w}'_i\| \|\mathbf{z}\| \cos \psi_i \cos \theta)}{\sum_k \exp(\|\mathbf{w}'_k\| \|\mathbf{z}\| \cos \psi_k \cos \theta)}, \quad (7)$$

Recall the fact that rotation transformation does not change the vector norm and the norm of vectors are non-negative, $\hat{P}_X - \hat{P}'_X > 0$ when $0^\circ < \theta < 90^\circ$.

□

The actual distribution of the data when the rotation transformation is applied is illustrated in Fig. 3. This figure depicts the distribution of $\angle(\mathbf{w}_i, \mathbf{z}_x)$. Formally, we denote data pair as $(x, y) \in \mathcal{X} \times \mathcal{Y}$, penultimate feature as \mathbf{z}_x , original weight as \mathbf{W} , tilted weight $\mathbf{W}^1 = R_1 \mathbf{W} = [\mathbf{w}_1^1 \mathbf{w}_2^1 \dots \mathbf{w}_C^1]$ where $mRC(\mathbf{W}, R_1) = 30^\circ$, tilted weight of $mRC=45^\circ$ as $\mathbf{W}^2 = R_2 \mathbf{W} = [\mathbf{w}_1^2 \mathbf{w}_2^2 \dots \mathbf{w}_C^2]$ where $mRC(\mathbf{W}, R_2) = 45^\circ$. For distribution depicted *Orig.* we plot $\angle(\mathbf{w}_y, \mathbf{z}_x)$ for the samples. For the 30° , and 45° , we plot $\angle(\mathbf{w}_y^1, \mathbf{z}_x)$ and $\angle(\mathbf{w}_y^2, \mathbf{z}_x)$ respectively. For the “False” plot, we randomly choose a class $y' \neq y$, and compute the $\angle(\mathbf{w}_{y'}, \mathbf{z}_x)$. We randomly sampled 4,000 data from the test dataset. We conducted this experiment on three benchmark datasets, namely CIFAR10, CIFAR100, and ImageNet. For each dataset, we

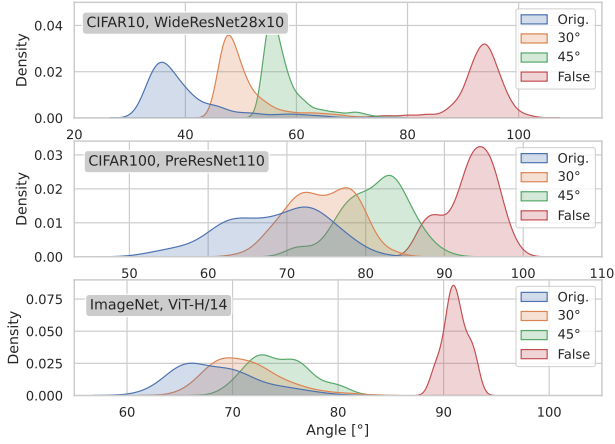


Figure 3. Distribution plot of the data samples with angle between class vector and pf, $\angle(\mathbf{w}_i, \mathbf{z}_x)$, with the corresponding predicted class row vector of the **original weight** (Orig.) and the **tilted weights** by depicted angle of mRC , 30° , 45° . “False” denotes the angle of pf with the class vector does not correspond to the respective class. As the mRC increases, the angles shift towards 90° . The distributions of various dataset-architectures can be observed in the appendix, specifically in Fig. 7 and 8. The visuals are enhanced with colors.

respectively plotted the distribution for WideResNet28x10, PreResNet110, and ViT-H/14 architectures. Experimentally, we demonstrate the capability to modify angles using the algorithm depicted in this distribution plot across various datasets and models. Specifically, as mRC increases, it can be observed that the angle distribution gradually shifts towards 90 degrees.

3.2. ”AVERAGE” tilted weights for Accuracy Compensation.

As evident from Fig. 3, adjusting angles through the proposed algorithm can lead to overlap with the distribution of the false class, eventually resulting in a lack of separability for the classifier. This, in turn, may lead to a deterioration in the overall performance of the classifier. Therefore, we propose to tune the network by weight averaging to address this issue. We simply apply weight averaging on the multiple tilted weights $\mathbf{W}^1, \dots, \mathbf{W}^{n_e}$ generated on $mRC = \theta$ as in Eq. 8, where n_e denotes the number of the tilted weights.

$$\mathbf{W}_{TNA} = \frac{1}{n_e}(\mathbf{W}^1 + \mathbf{W}^2 + \dots + \mathbf{W}^{n_e}), \quad (8)$$

In practice, we generate multiple rotation matrices R_1, \dots, R_{n_e} with the same number of n_r , and average to get the final transformation matrix R for computational simplicity as in Alg. 1-AVERAGE.

Vector Averaging on equally tilted weights. Weight Aver-

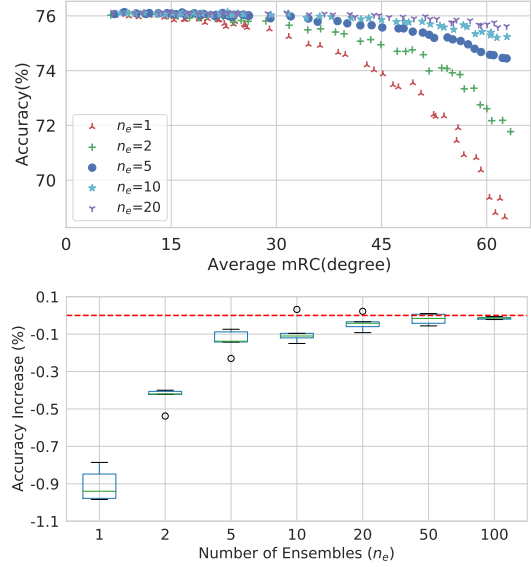


Figure 4. Plots of the accuracy of the ensembled outputs correspond to the number of ensemble members, on the ImageNet dataset. The accuracy is well compensated at most of the angles (upper) and as the n_e increases (lower). The red line indicates the performance of the original weight. The performance is averaged over 10 runs. Extended experiments at appendix Fig. 6

aging averages the *tilted class vectors* generated by equal mRC . This relieves the probability of collapsing in accuracy because weight averaging works as a *arithmetic mean* over $s_i = \mathbf{w}_i \cdot \mathbf{z}$, and *geometric mean* over the e^{s_i} , which are the softmax members if ignoring the bias. If the rotation happens to the unwanted direction, averaging weight acts as a geometric mean on the softmax member, and may compensate for the final score through statistical effects.

We illustrate the plot for the interpolated accuracy results through weight averaging in Figure 4. This experiment was conducted on the ImageNet dataset using the ResNet50 architecture. Initially, tilted weights with $mRC = \theta$ were generated, and for each of the generated tilted weights (totaling n_e), weight averaging was applied, and the corresponding accuracy was recorded. Each point in the plot represents the performance of the classifier when the averaged weight is applied. The upper plot presents the results of experiments conducted for different mRC s by varying n_e from 1 to 20, while the lower plot records the averaged accuracy for a fixed mRC of 30 degrees over a specified n_e for 1 to 100. Through this, we observe that as the intensity of the rotation transformation increases, there is a decline in accuracy, but this degradation can be interpolated through weight averaging. In other words, the proposed algorithm effectively interpolates accuracy under varying levels of rotation transformation intensity.

Algorithm 1 TILT AND AVERAGE (TNA)

Input: $mRC \theta^*$, original weight \mathbf{W}
Parameter: $n_e, n_t, \alpha, \beta, \theta_s$
Output: alternative weight \mathbf{W}'

 (1. (TILT) Rotation Transform of $mRC \theta^*$ Generation)

 $R_1 \leftarrow$ Identity Matrix $I_n, n_r \leftarrow 0$
while $mRC(\mathbf{W}, R_1) \leq \theta^*$ **do**
 $R^t \leftarrow$ Identity Matrix I_n
 $\tau \sim \text{Beta}(\alpha, \beta), \theta_t = \theta_s \times \tau, k_1, k_2 \in [n]$
 $R_{k_1 k_1}^t = \cos \theta_t, R_{k_1 k_2}^t = -\sin \theta_t$
 $R_{k_2 k_1}^t = \sin \theta_t, R_{k_2 k_2}^t = \cos \theta_t$
 $R_1 \leftarrow R_1 R^t$
 $n_r \leftarrow n_r + n_t$
end while

(2. (AVERAGE) Compensate Accuracy)

 Repeat Procedure (1) n_e times and get R_1, R_2, \dots, R_{n_e}
 $R \leftarrow \frac{1}{n_e}(R_1 + R_2 + \dots + R_{n_e})$
 $\mathbf{W}' \leftarrow R\mathbf{W}$
return \mathbf{W}'

4. Experiments

4.1. Evaluation Metrics

We report the Accuracy, ECE, and AdaECE in % in table 1. In practice, the Calibration Error is intractable since the joint distribution $\mathbb{P}(X, Y)$ is unknown. To evaluate the calibration performance of the classifiers, we estimate Calibration Error (noted in Section 2.2) by 2 different schemes, **ECE** and **AdaECE**. We also display the accuracy as well, to demonstrate the accuracy change after applying TNA.

Expected Calibration Error, or **ECE**, estimates Calibration Error by *equal-interval-binning* scheme. Suppose there exists B bins of $|D|$ data samples, where each bin $B_j, j \in \{0, 1, \dots, B-1\}$ consists of the samples with confidence corresponding to the interval $I_j = \left(\frac{j}{B}, \frac{j+1}{B}\right]$. Then, **ECE** = $\sum_j \frac{|B_j|}{|D|} |acc(B_j) - conf(B_j)|$, where $acc(B_j)$ is the accuracy of the samples from B_j , and $conf(B_j)$ is the average confidence of the samples from B_j (Naeini et al., 2015).

Adaptive Expected Calibration Error, or **AdaECE**, estimates Calibration Error by *uniform-mass-binning* scheme, with identical number of samples for each bin (Mukhoti et al., 2020). In other words, **AdaECE** = $\sum_j \frac{|B_j|}{|D|} |acc(B_j) - conf(B_j)|$ where each bin B_j is set to include $\frac{|D|}{B}$ samples with the ascending order of the confidence value.

4.2. Experimental Details

Datasets. We report the results of the proposed method on 4 different image classification datasets. The number at the end represents the number of samples used for train-

ing/calibration/test split. The number of splits for each data partition adheres to the methodology outlined in the work of Ashukha et al. (2020).

- CIFAR10, CIFAR100 (Krizhevsky et al., 2010): Tiny images from web. 10 and 100 classes respectively. 50,000/5,000/5,000
- ImageNet-1k (Deng et al., 2009) : Image of natural objects, 1000 classes, 1.2M/12,500/37,500
- SVHN (Netzer et al., 2011): Street View House Numbers, 10 classes of digits, 73,257/5,000/19,032. Results in the appendix, Tab. 2.

Models. We compare a total of four model architectures for each dataset. For datasets SVHN and CIFARs, we take the models of WideResNet28x10 (Zagoruyko & Komodakis, 2016), MobileNetV2 (Sandler et al., 2018), PreResNet110 (He et al., 2016b), and GoogleNet (Szegedy et al., 2015). For ImageNet, we take 2 CNNs, ResNet-50 (He et al., 2016a), and 2 visual transformers ViT-L/16, ViT-H/14 (Dosovitskiy et al., 2021). For the ImageNet trained networks, the models are borrowed from torchvision (Marcel & Rodriguez, 2010) and timm (Wightman, 2019). For the other datasets, we follow the training details from (Ashukha et al., 2020), which are listed in the appendix.

Methods. For each dataset-model combination, we evaluate five baselines, including the uncalibrated model, and additionally assess nine methods with the proposed technique TNA, presented in this paper. The optimization is done by the calibration split, and the evaluation is done on the test split. The code will be available, [URL](#).

- Baseline Method : We apply the proposed method on the original weight, in combination with the calibration-map-based methods of IROvA (Zadrozny & Elkan, 2001), Temperature Scaling (TS) (Guo et al., 2017), Ensemble Temperature Scaling (ETS) (Zhang et al., 2020), and Atypicality-Aware Recalibration (AAR) (Yuksekgonul et al., 2023).
- TNA, TNA(Sparse) : TNA, TNA(Sparse) reveals outcomes achieved by optimizing each of the two steps independently: first, the alternative weight \mathbf{W}' , and subsequently, the calibration map f_{cal} . In the quest for the optimal alternative weight \mathbf{W}' , the initial step involves searching for the best angle mRC within the range $[0^\circ, 90^\circ]$ using the calibration set. As indicated in Proposition 3.3, an increase in mRC results in relaxed confidence, rendering the ECE plot unimodal with mild assumptions into account. This can also be confirmed experimentally. Refer to Fig. 9 for detailed plots of the optimization curves on CIFAR10, CIFAR100, and ImageNet. Computationally, this process takes less than

Table 1. Main results displaying changes after TNA, in accuracy and calibration performance. The experiments were conducted on CIFAR10, CIFAR100, and ImageNet datasets, evaluating four different model architectures for each dataset. In addition to applying five recalibration techniques, including the uncalibrated model as a baseline, we evaluate TNA(sparse) and TNA(comp.), which involve two stages of optimization and explore the entire search space, respectively. The results are displayed as averages over five runs. In a specific dataset-model combination, indicate the technique that achieved the best results among all methods in **bold**. Lower ECE, AdaECE, the better.

CIFAR10-WideResNet28x10				CIFAR10-MobileNetV2			CIFAR10-PreResNet110			CIFAR10-GoogleNet		
Methods	Acc. (↑)	ECE (↓)	AdaECE (↓)	Acc. (↑)	ECE (↓)	AdaECE (↓)	Acc. (↑)	ECE (↓)	AdaECE (↓)	Acc. (↑)	ECE (↓)	AdaECE (↓)
None	96.37 ₁₅	1.66 ₁	1.49 ₀₉	92.51 ₂₆	3.49 ₁₆	3.33 ₂₄	95.28 ₁₅	2.67 ₁₃	2.62 ₁₄	95.16 ₂₂	2.82 ₁₉	2.75 ₂₁
+TNA	96.37 ₁₆	0.66 ₁₄	0.59 ₁	92.55 ₂₅	0.78 ₁₇	0.65 ₂₄	95.28 ₁₁	0.76 ₀₃	0.4 ₀₄	95.17 ₂₁	1.57 ₁₈	1.59 ₂₁
IROvA	96.29 ₁₉	0.83 ₂₉	0.56 ₁₁	92.39 ₂₄	1.24 ₁₅	0.92 ₂₉	95.16 ₀₉	0.88 ₁₂	0.73 ₁₁	95.11 ₁₈	1.01 ₂₅	0.96 ₀₈
+TNA(sparse)	96.32 ₁₆	0.83 ₂₃	0.55 ₂₄	92.39 ₂₉	1.22 ₁₃	0.87 ₃₂	95.31 ₀₄	0.74 ₀₈	0.4 ₁₉	95.07 ₁₆	0.96 ₂₆	0.85 ₀₉
+TNA(comp.)	96.32 ₁₃	0.8 ₂	0.62 ₁₈	92.5 ₁₉	1.18 ₂₂	0.89 ₂	95.31 ₀₄	0.74 ₀₈	0.4 ₁₉	95.07 ₁₆	0.96 ₂₆	0.85 ₀₉
TS	96.37 ₁₅	0.84 ₀₅	0.71 ₂₂	92.51 ₂₆	1.06 ₁₉	0.88 ₂₇	95.28 ₁₅	0.73 ₀₉	0.65 ₁₂	95.16 ₂₂	2.14 ₁₃	1.63 ₃
+TNA(sparse)	96.37 ₁₆	0.78 ₁₃	0.75 ₂	92.55 ₂₅	0.81 ₁₂	0.72 ₂₅	95.28 ₁₁	0.68 ₀₉	0.41 ₀₃	95.17 ₂₁	2.09 ₁₆	1.64 ₃₁
+TNA(comp.)	96.39 ₁₂	0.71 ₁₄	0.53 ₀₆	92.54 ₁₉	0.79 ₀₉	0.76 ₁₉	95.13 ₁₈	0.65 ₁₁	0.45 ₁₁	95.08 ₁₆	1.96 ₁	1.58 ₁₃
ETS	96.37 ₁₅	0.84 ₀₆	0.79 ₁₉	92.51 ₂₆	0.85 ₁₉	0.67 ₂₄	95.28 ₁₅	0.67 ₁	0.5 ₁₂	95.16 ₂₂	2.14 ₁₃	1.63 ₃
+TNA(sparse)	96.37 ₁₆	0.78 ₁₄	0.72 ₁₇	92.55 ₂₅	0.83 ₀₉	0.71 ₂₆	95.28 ₁₁	0.69 ₀₈	0.42 ₀	95.17 ₂₁	2.09 ₁₆	1.64 ₃₁
+TNA(comp.)	96.39 ₁₂	0.71 ₁₄	0.53 ₀₆	92.56 ₂	0.79 ₁	0.82 ₂₅	94.66 ₁₈	0.65 ₁₁	0.45 ₁₁	95.08 ₁₆	1.96 ₁	1.58 ₁₃
AAR	96.33 ₂	0.75 ₀₈	0.45 ₀₉	92.38 ₃₂	0.91 ₀₇	e0.67 ₁	95.17 ₀₈	0.59 ₁	0.45 ₀₅	95.14 ₂₄	1.04 ₁₂	0.95 ₁₉
+TNA(sparse)	96.35 ₁₉	0.72 ₀₅	0.45 ₀₈	92.37 ₃₃	0.83 ₁₄	0.64 ₁₂	95.3 ₁₃	0.59 ₁₈	0.34 ₁₃	95.12 ₂₆	0.98 ₁₇	0.95 ₂₂
+TNA(comp.)	96.41 ₁₈	0.72 ₂₃	0.44 ₁₉	92.37 ₃₃	0.83 ₁₄	0.64 ₁₂	94.99 ₁	0.56 ₁₃	0.34 ₀₈	95.12 ₂₂	0.9 ₀₁	0.95 ₂₂
CIFAR100-WideResNet28x10				CIFAR100-MobileNetV2			CIFAR100-PreResNet110			CIFAR100-GoogleNet		
Methods	Acc. (↑)	ECE (↓)	AdaECE (↓)	Acc. (↑)	ECE (↓)	AdaECE (↓)	Acc. (↑)	ECE (↓)	AdaECE (↓)	Acc. (↑)	ECE (↓)	AdaECE (↓)
None	80.42 ₄₇	5.91 ₃	5.77 ₄	72.79 ₁₄	10.03 ₁₉	9.97 ₁₈	77.69 ₃₅	10.62 ₃₃	10.58 ₃₄	79.42 ₂₆	6.45 ₂	6.3 ₁₉
+TNA	80.17 ₅₃	4.11 ₁₉	3.92 ₁₅	72.71 ₁₃	1.54 ₀₉	1.52 ₁₉	77.15 ₃₄	2.97 ₂₅	2.84 ₂₉	79.36 ₂₅	3.86 ₂	3.86 ₁₆
IROvA	80.69 ₃₆	4.71 ₁₄	4.27 ₁₅	72.15 ₂₂	4.81 ₂₈	4.79 ₁₉	76.95 ₂₅	3.7 ₁₇	4.7 ₄₉	78.92 ₂₇	3.73 ₃₅	4.68 ₁₇
+TNA(sparse)	80.4 ₄₃	4.15 ₂₆	3.36 ₃₅	72.01 ₂₆	4.72 ₂₉	4.17 ₂₅	76.51 ₂₂	3.91 ₂	3.65 ₆₁	78.88 ₃₅	3.66 ₃₅	3.23 ₁₇
+TNA(comp.)	81.11 ₃	3.89 ₁₁	3.35 ₁₄	72.45 ₃₆	4.32 ₁₄	3.91 ₃₈	76.93 ₃	3.66 ₄₉	3.6 ₄₇	78.88 ₃₅	3.66 ₃₅	3.23 ₁₇
TS	80.42 ₄₇	4.69 ₂₂	4.55 ₂₆	72.79 ₁₄	1.82 ₃₃	1.78 ₁₁	77.69 ₃₅	3.21 ₁₇	3.13 ₁₇	79.42 ₂₆	4.27 ₁₂	4.28 ₁₅
+TNA(sparse)	80.17 ₂₃	4.55 ₂₄	4.28 ₁₄	72.71 ₁₃	1.41 ₁₅	1.34 ₁₁	77.15 ₃₄	3.16 ₂₆	3.03 ₃₅	79.36 ₂₅	4.23 ₁₄	4.13 ₁₈
+TNA(comp.)	80.17 ₅₃	4.55 ₂₄	4.28 ₁₄	73.13 ₂	1.41 ₃₃	1.24 ₃₃	75.64 ₆₄	3.01 ₁₅	2.97 ₁₄	79.36 ₂₅	4.23 ₁₄	4.13 ₁₈
ETS	80.42 ₄₇	3.47 ₂₈	3.88 ₂₁	72.79 ₁₄	1.63 ₃₉	1.56 ₁₂	77.97 ₄₄	2.38 ₃₇	2.6 ₃₃	79.42 ₂₆	3.25 ₁₉	3.4 ₂₂
+TNA(sparse)	80.17 ₅₃	3.35 ₂₆	3.89 ₂₂	72.71 ₁₃	1.22 ₁₈	1.32 ₀₃	77.15 ₃₄	2.19 ₂₈	2.49 ₃₅	79.36 ₂₅	2.86 ₂	3.35 ₂₆
+TNA(comp.)	80.76 ₂₇	3.06 ₁₆	3.52 ₁₇	73.13 ₂	1.27 ₃₂	1.18 ₂₉	75.74 ₇₂	2.13 ₂₇	2.4 ₃₇	79.36 ₂₅	2.86 ₂	3.35 ₂₆
AAR	81.06 ₁₄	3.4 ₃₈	3.19 ₃₃	72.53 ₁₇	2.06 ₄	1.82 ₄₄	77.37 ₃₇	3.27 ₁₂	3.23 ₂₁	79.28 ₃	4.46 ₃₁	4.28 ₃
+TNA(sparse)	80.98 ₂₂	3.33 ₄	3.15 ₃₃	72.39 ₂₆	1.95 ₃₉	1.85 ₃₃	77.15 ₄₇	3.36 ₂₂	3.07 ₁₈	79.38 ₂₉	4.45 ₂₃	4.34 ₂₈
+TNA(comp.)	80.98 ₂₂	3.33 ₄	3.15 ₃₃	73.09 ₂₆	1.52 ₁₇	1.47 ₂₇	76.83 ₄₂	3.15 ₄₁	2.87 ₄₃	78.91 ₁₈	4.45 ₀₅	4.27 ₂₅
ImageNet-ResNet50				ImageNet-DenseNet169			ImageNet-ViT-L/16			ImageNet-ViT-H/14		
Methods	Acc. (↑)	ECE (↓)	AdaECE (↓)	Acc. (↑)	ECE (↓)	AdaECE (↓)	Acc. (↑)	ECE (↓)	AdaECE (↓)	Acc. (↑)	ECE (↓)	AdaECE (↓)
None	76.17 ₀₅	3.83 ₀₉	3.73 ₁	75.63 ₁₁	5.43 ₀₈	5.43 ₀₈	84.35 ₀₆	1.81 ₀₇	1.8 ₀₉	85.59 ₀₅	1.87 ₀₇	1.77 ₀₇
+TNA	76.11 ₀₆	1.73 ₀₆	1.76 ₀₈	75.46 ₁₁	1.63 ₁₄	1.66 ₁₄	84.34 ₀₇	1.11 ₀₅	1.11 ₀₅	85.5 ₀₃	1.05 ₀₁	1.06 ₀₃
IROvA	74.96 ₀₇	6.23 ₃₇	5.63 ₂₉	74.82 ₁₃	6.19 ₇₇	5.72 ₅₄	83.5 ₁	5.35 ₂₉	4.27 ₁₄	84.75 ₀₃	5.3 ₁₆	4.31 ₃
+TNA(sparse)	74.87 ₀₅	6.24 ₁₉	4.58 ₃₃	74.49 ₂₃	6.1 ₇₂	4.71 ₆₇	83.41 ₁₁	5.32 ₂₉	4.05 ₁₂	84.54 ₀	5.24 ₂	4.0 ₂₄
+TNA(comp.)	74.98 ₀₃	6.03 ₁₁	4.55 ₂₁	74.41 ₁₃	6.05 ₆₁	4.7 ₅₆	83.72 ₀₈	5.16 ₁₁	4.05 ₀₁	84.43 ₁₃	5.17 ₁₁	3.9 ₁₆
TS	76.17 ₀₅	2.09 ₃	2.02 ₂₃	75.63 ₁₁	1.85 ₁	1.83 ₀₇	84.35 ₀₆	1.35 ₀₈	1.35 ₀₈	85.59 ₀₅	1.33 ₁₈	1.32 ₁₉
+TNA(sparse)	76.11 ₀₆	2.02 ₂₇	2.0 ₂₅	75.46 ₁₁	1.78 ₀₅	1.77 ₀₅	84.34 ₀₇	1.31 ₁₂	1.31 ₀₈	85.5 ₀₃	1.34 ₁₆	1.28 ₁₈
+TNA(comp.)	76.08 ₂₆	1.93 ₁₁	1.89 ₀₄	75.45 ₁₆	1.78 ₁₃	1.78 ₀₇	84.48 ₁₃	1.25 ₀₄	1.3 ₁₆	85.48 ₁₅	1.31 ₁₁	1.23 ₀₁
ETS	76.17 ₀₅	1.1 ₀₃	1.26 ₁	75.63 ₁₁	0.88 ₁₁	1.06 ₁₉	84.35 ₀₆	0.95 ₀₆	1.14 ₀₆	85.59 ₀₅	0.63 ₁₃	0.91 ₁₃
+TNA(sparse)	76.11 ₀₆	1.06 ₀₅	1.22 ₀₆	75.46 ₁₁	0.79 ₁₃	1.02 ₁₂	84.34 ₀₇	0.9 ₀₅	1.09 ₀₆	85.5 ₀₃	0.6 ₁₄	0.85 ₁₄
+TNA(comp.)	76.04 ₁₁	1.01 ₁₅	1.19 ₀₃	75.45 ₂₃	0.78 ₁₁	1.01 ₁₄	84.5 ₁₁	0.9 ₁₇	1.1 ₁₁	85.43 ₁₂	0.6 ₀₅	0.84 ₀₇
AAR	75.55 ₀₅	2.53 ₁₇	2.5 ₁₇	75.37 ₀₉	2.2 ₂₂	2.2 ₂₈	83.93 ₀₈	2.43 ₁₅	2.4 ₁₄	84.96 ₁₃	2.36 ₂₈	2.2 ₃₇
+TNA(sparse)	75.48 ₀₄	2.52 ₂	2.49 ₂	75.23 ₁₅	2.33 ₂	2.22 ₂₁	83.93 ₀₇	2.41 ₁₅	2.38 ₁₄	84.9 ₁₄	2.3 ₃₄	2.25 ₃
+TNA(comp.)	75.36 ₂₃	2.40 ₂₁	2.39 ₁₁	75.17 ₁₈	2.28 ₁₁	2.25 ₀₇	84.2 ₀₇	2.38 ₀₄	2.38 ₁₁	84.81 ₁₂	2.32 ₀₃	2.28 ₀₅

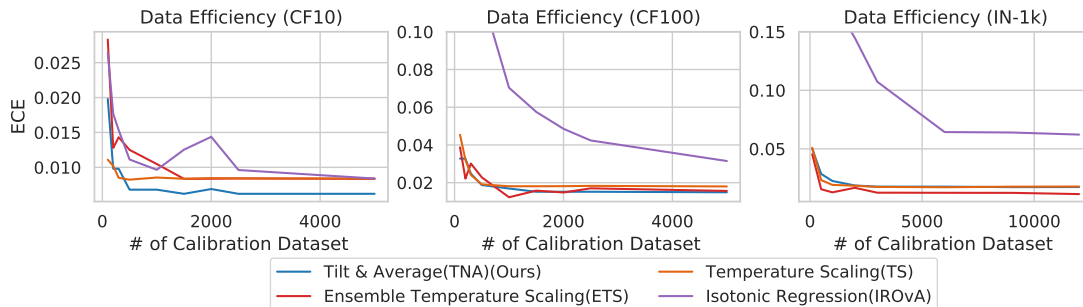


Figure 5. The data efficiency plot comparing 3 datasets(CIFAR10, CIFAR100, ImageNet). The architectures of WideResNet28x10, MobileNetv2, and ResNet50 are used respectively, when TNA is applied to the original weight. We demonstrate that TNA is efficient in data, requiring less additional calibration set.

5 minutes on a single GPU of RTX3080. (CIFAR10, and CIFAR100 take seconds.)

- TNA(Comp.) : For the complete search, we aim to search for the best combination of the alternative weights and the selected calibration-map-based method. Using the calibration dataset, we perform a grid search for all possible (\mathbf{W}', f_{cal}) pairs. Computationally, this process takes less than 30 minutes on a single GPU of RTX3080. (CIFAR10, CIFAR100 takes a few minutes.)

Hyperparameters. As proposed in the algorithm, we search over $\theta \in [0^\circ, 90^\circ]$. Over datasets and models, n_e is set to 10, $\alpha = 5$, $\beta = 1$. The search interval of rotation number n_t is set to 50. Unless noted, the maximum rotated angle θ_s is set to 0.9rad. The displayed value reflects an average of 5 repeated experiments, with the standard deviation depicted as a subscripted value. The number of bins B is set to 15.

4.3. Results

The classifier weights newly derived through TNA do induce a very slight change in accuracy, albeit very marginal (less than 0.3%). In terms of calibration performance, the application of weights by TNA surpasses the performance of using the original weight. Also in most cases, applying TNA in addition to the method improves performance than the case of applying the calibration-map-based method alone. The results indicate that, in addition to the conventional method of finding f_{cal} , it offers a broader solution space.

One interesting observation is that the combination of None+TNA, which only applies to adjust to the angle, outperforms Temperature Scaling. As highlighted in Section 5, temperature scaling can be seen as adjusting for magnitude, and it is evident that adjusting for angles is particularly effective in cases where it matters.

Note that the TS and ETS do not affect the accuracy, while

IROvA and AAR slightly have different values. This is because TS and ETS preserve the order of the class-wise element of the logit vector. On the contrary, the approaches of IROvA and AAR may exhibit a slight variation in accuracy, as the final probability is adjusted due to factors that can alter the order.

4.4. Ablation Study

Data Efficiency. Assessing data efficiency is also an important aspect (Zhang et al., 2020) to make the calibration process utilizable since recalibration requires an additional 'calibration set' other than a 'training set' to tune the probability. According to Fig. 5, note that TS(Guo et al., 2017) and the TNA show similar data efficiency to reach the optimal ECE while exhibiting better efficiency than IROvA(Zadrozny & Elkan, 2002). One explanation for the observed phenomenon is that for TNA, we optimize a single parameter $\theta(mRC)$, similar to that of TS, in which we also optimize a single parameter T (temperature).

Assumptions. In our study, various assumptions were made to demonstrate that the algorithm has confidence calibration effects. We reiterate some of the assumptions and provide deeper explanations. In detail, we elucidate the assumptions of 1) $\angle(\mathbf{w}_i, R\mathbf{w}_i)$ is equal across classes $i \in [C]$, and 2) the feature space is high-dimensional with experimental results in the Appendix B.

5. Discussion & More Related Works

Scaling Angles. From a geometrical standpoint, we provide a technique that directly controls the angles. The role of the angle as a similarity/distance measure has been discussed in previous research (Kansizoglou et al., 2022; Chen et al., 2020; Kang et al., 2020; Peng et al., 2022). However, to our knowledge, our paper is the first to introduce a geometric transformation that alters the angle between the class vector and the penultimate feature to adjust the confidence.

Recalibration Approaches with Magnitude. The magnitude of the class vector also influences the confidence factor (Eq. 2). Upon closer examination, this approach shares common ground with previously studied methods such as temperature scaling (Guo et al., 2017). As a straightforward proposition, temperature scaling applies scalar division on the logit vector \mathbf{s} to obtain confidence. Substituting the \mathbf{w}_i as \mathbf{w}_i/T , finding the optimal temperature has the effect of confidence relaxation by adjusting the magnitude. ETS (Zhang et al., 2020) and AAR (Yuksekgonul et al., 2023) extend the concept of temperature scaling by seeking the optimal temperature sample-wise, considering the diversity of samples.

Blessings of the dimensionality. Our approach is founded upon a modicum of randomness as it pursues a rotation transformation. Due to the *blessings of the dimensionality* (n of few hundred or thousands), we have a very low probability to rotate to the unwanted direction, where other class vectors might gain their score significantly and the overconfident vector loses it. From the high dimensional geometry (Blum et al., 2020), it is known that most of the volume is concentrated on the equator and the surface, and thus two arbitrary vectors are likely to be orthogonal. For example, in 2000-dimensional unit-ball, the volume near the equator of height $\frac{1}{2}$ is near $1 - \frac{2}{10\sqrt{5}}e^{-\frac{1}{2}*(10\sqrt{5}^2)} \simeq (100 - 3.4 * 10^{-105})\%$ of the whole volume. So the single row vector \mathbf{w}_i from the perspective of the \mathbf{z} which has angle $\angle(\mathbf{w}_i, \mathbf{z})$ near 60° with a perturbation of some angle is more likely to lean toward the equator, not the direction toward the \mathbf{z} . Note that ResNet-50, the dimension of the \mathbf{z} space is 2048, $\cos 60^\circ = \frac{1}{2}$.

6. Conclusion

We introduce a fresh perspective on tackling the longstanding issue of recalibration by geometrically modifying the weights of the last layer instead of proposing a new calibration map for better calibration performance. We propose a new algorithm from this perspective, establish its theoretical background, and experimentally validate it. The presented technique outperforms existing methods.

7. Broader Impact

This paper presents work whose goal is to advance the field of Machine Learning. There are many potential societal consequences of our work, none which we feel must be specifically highlighted here.

Acknowledgements

This work was partially supported by Korea Institute of Marine Science & Technology Promotion (KIMST) funded by the Korea Coast Guard (RS-2023-00238652, Integrated

Satellite-based Applications Development for Korea Coast Guard). Also, this work was partially supported by Korea Research Institute for defense Technology planning and advancement – Grant funded by Defense Acquisition Program Administration (DAPA) (KRIT-CT-23-020)

Impact Statement

This paper presents work whose goal is to advance the field of Machine Learning. There are many potential societal consequences of our work, none which we feel must be specifically highlighted here.

References

- Ashukha, A., Lyzhov, A., Molchanov, D., and Vetrov, D. Pitfalls of in-domain uncertainty estimation and ensembling in deep learning. *arXiv preprint arXiv:2002.06470*, 2020.
- Blum, A., Hopcroft, J., and Kannan, R. *Foundations of Data Science*. Cambridge University Press, 2020. doi: 10.1017/9781108755528.
- Chen, B., Liu, W., Yu, Z., Kautz, J., Shrivastava, A., Garg, A., and Anandkumar, A. Angular visual hardness. In *Proceedings of the 37th International Conference on Machine Learning, ICML 2020, 13-18 July 2020, Virtual Event*, volume 119 of *Proceedings of Machine Learning Research*, pp. 1637–1648. PMLR, 2020. URL <http://proceedings.mlr.press/v119/chen20n.html>.
- Daniel Kermany, Kang Zhang, M. G. Labeled optical coherence tomography (oct) and chest x-ray images for classification. *Mendeley Data*, 2018.
- Deng, J., Dong, W., Socher, R., Li, L.-J., Li, K., and Fei-Fei, L. ImageNet: A large-scale hierarchical image database. In *CVPR*, 2009.
- Ding, Z., Han, X., Liu, P., and Niethammer, M. Local temperature scaling for probability calibration. In *Proceedings of the IEEE/CVF International Conference on Computer Vision*, pp. 6889–6899, 2021.
- Dosovitskiy, A., Beyer, L., Kolesnikov, A., Weissenborn, D., Zhai, X., Unterthiner, T., Dehghani, M., Minderer, M., Heigold, G., Gelly, S., Uszkoreit, J., and Hounsby, N. An image is worth 16x16 words: Transformers for image recognition at scale. In *ICLR*, 2021.
- Euler, L. *Novi commentarii Academiae Scientiarum Imperialis Petropolitanae*, volume 20. Petropolis, Typis Academiae Scientiarum, 1750-76, 1776.

- Garipov, T., Izmailov, P., Podoprikin, D., Vetrov, D., and Wilson, A. G. Loss surfaces, mode connectivity, and fast ensembling of dnns. In *Proceedings of the 32nd International Conference on Neural Information Processing Systems*, NIPS'18, pp. 8803–8812, Red Hook, NY, USA, 2018. Curran Associates Inc.
- Givens, W. Computation of plane unitary rotations transforming a general matrix to triangular form. *Journal of the Society for Industrial and Applied Mathematics*, 6(1):26–50, 1958. ISSN 03684245. URL <http://www.jstor.org/stable/2098861>.
- Guo, C., Pleiss, G., Sun, Y., and Weinberger, K. Q. On calibration of modern neural networks. In *Proceedings of the 34th International Conference on Machine Learning - Volume 70*, ICML'17, pp. 1321–1330. JMLR.org, 2017.
- He, K., Zhang, X., Ren, S., and Sun, J. Deep residual learning for image recognition. In *CVPR*, 2016a.
- He, K., Zhang, X., Ren, S., and Sun, J. Identity mappings in deep residual networks, 2016b. URL <http://arxiv.org/abs/1603.05027>. cite arxiv:1603.05027Comment: ECCV 2016 camera-ready.
- Huang, G., Liu, Z., Van Der Maaten, L., and Weinberger, K. Q. Densely connected convolutional networks. In *CVPR*, 2017.
- Hub, A. Mono and Colored Egg Data. <https://www.aihub.or.kr/aihubdata/data/view.do?currMenu=115&topMenu=100&dataSetSn=71504>, 2022.
- Joy, T., Pinto, F., Lim, S.-N., Torr, P. H. S., and Dokania, P. K. Sample-dependent adaptive temperature scaling for improved calibration. In *Proceedings of the Thirty-Seventh AAAI Conference on Artificial Intelligence and Thirty-Fifth Conference on Innovative Applications of Artificial Intelligence and Thirteenth Symposium on Educational Advances in Artificial Intelligence*, AAAI'23/IAAI'23/EAAI'23. AAAI Press, 2023. ISBN 978-1-57735-880-0. doi: 10.1609/aaai.v37i12.26742. URL <https://doi.org/10.1609/aaai.v37i12.26742>.
- Kang, B., Xie, S., Rohrbach, M., Yan, Z., Gordo, A., Feng, J., and Kalantidis, Y. Decoupling representation and classifier for long-tailed recognition. In *8th International Conference on Learning Representations, ICLR 2020, Addis Ababa, Ethiopia, April 26-30, 2020*. OpenReview.net, 2020. URL <https://openreview.net/forum?id=r1gRTCvFvB>.
- Kansizoglou, I., Bampis, L., and Gasteratos, A. Deep feature space: A geometrical perspective. *IEEE Trans. Pattern Anal. Mach. Intell.*, 44(10Part2):6823–6838, oct 2022. ISSN 0162-8828. doi: 10.1109/TPAMI.2021.3094625. URL <https://doi.org/10.1109/TPAMI.2021.3094625>.
- Krizhevsky, A., Nair, V., and Hinton, G. Cifar-10 (canadian institute for advanced research). URL <http://www.cs.toronto.edu/kriz/cifar.html>, 2010.
- Kull, M., Perello-Nieto, M., Kängsepp, M., Filho, T. S., Song, H., and Flach, P. *Beyond Temperature Scaling: Obtaining Well-Calibrated Multiclass Probabilities with Dirichlet Calibration*. Curran Associates Inc., Red Hook, NY, USA, 2019.
- Li, Y. and Vasconcelos, N. Efficient multi-domain learning by covariance normalization. In *CVPR*, 2019.
- Litjens, G., Kooi, T., Bejnordi, B. E., Setio, A. A. A., Ciompi, F., Ghafoorian, M., van der Laak, J. A., van Ginneken, B., and Sánchez, C. I. A survey on deep learning in medical image analysis. *Medical Image Analysis*, 42:60–88, 2017. ISSN 1361-8415. doi: <https://doi.org/10.1016/j.media.2017.07.005>. URL <https://www.sciencedirect.com/science/article/pii/S1361841517301135>.
- Ma, X. and Blaschko, M. B. Meta-cal: Well-controlled post-hoc calibration by ranking. In *International Conference on Machine Learning*, 2021.
- Marcel, S. and Rodriguez, Y. Torchvision the machine-vision package of torch. pp. 1485–1488, 10 2010. doi: 10.1145/1873951.1874254.
- Moskolai, W. R., Abdou, W., and Dipanda, A. Application of deep learning architectures for satellite image time series prediction: A review. *Remote Sensing*, 13(23): 4822, 2021.
- Mukhoti, J., Kulharia, V., Sanyal, A., Golodetz, S., Torr, P. H., and Dokania, P. K. Calibrating deep neural networks using focal loss. 2020.
- Naeini, M., Cooper, G., and Hauskrecht, M. Obtaining well calibrated probabilities using bayesian binning. *Proceedings of the AAAI Conference on Artificial Intelligence*, 29(1), Feb. 2015. doi: 10.1609/aaai.v29i1.9602. URL <https://ojs.aaai.org/index.php/AAAI/article/view/9602>.
- Netzer, Y., Wang, T., Coates, A., Bissacco, A., Wu, B., and Ng, A. Y. Reading digits in natural images with unsupervised feature learning. In *NeurIPS*, 2011.
- Ovadia, Y., Fertig, E., Ren, J., Nado, Z., Sculley, D., Nowozin, S., Dillon, J. V., Lakshminarayanan, B., and Snoek, J. *Can You Trust Your Model's Uncertainty?*

- Evaluating Predictive Uncertainty under Dataset Shift*. Curran Associates Inc., Red Hook, NY, USA, 2019.
- Patel, Beluch, W., Yang, B., Pfeiffer, M., and Zhang, D. Multi-class uncertainty calibration via mutual information maximization-based binning. In *International Conference on Learning Representations (ICLR)*, 2021.
- Peng, B., Islam, M., and Tu, M. Angular gap: Reducing the uncertainty of image difficulty through model calibration. In *Proceedings of the 30th ACM International Conference on Multimedia, MM '22*, pp. 979–987, New York, NY, USA, 2022. Association for Computing Machinery. ISBN 9781450392037. doi: 10.1145/3503161.3548289. URL <https://doi.org/10.1145/3503161.3548289>.
- Platt, J. Probabilities for sv machines. pp. 61–74, 01 1999.
- Rahimi, A., Shaban, A., Cheng, C.-A., Hartley, R., and Boots, B. Intra order-preserving functions for calibration of multi-class neural networks. In *Proceedings of the 34th International Conference on Neural Information Processing Systems, NeurIPS'20*, Red Hook, NY, USA, 2020. Curran Associates Inc. ISBN 9781713829546.
- Sandler, M., Howard, A. G., Zhu, M., Zhmoginov, A., and Chen, L. Mobilenetv2: Inverted residuals and linear bottlenecks. In *2018 IEEE Conference on Computer Vision and Pattern Recognition, CVPR 2018, Salt Lake City, UT, USA, June 18-22, 2018*, pp. 4510–4520. Computer Vision Foundation / IEEE Computer Society, 2018. doi: 10.1109/CVPR.2018.00474. URL http://openaccess.thecvf.com/content_cvpr_2018/html/Sandler_MobileNetV2_Inverted_Residuals_CVPR_2018_paper.html.
- Szegedy, C., Liu, W., Jia, Y., Sermanet, P., Reed, S., Anguelov, D., Erhan, D., Vanhoucke, V., and Rabinovich, A. Going deeper with convolutions. In *CVPR*, 2015.
- Tomani, C., Cremers, D., and Buettner, F. Parameterized temperature scaling for boosting the expressive power in post-hoc uncertainty calibration. In *European Conference on Computer Vision*, 2022.
- Wenger, J., Kjellström, H., and Triebel, R. Non-parametric calibration for classification. AISTATS'20, 08 2020.
- Wightman, R. Pytorch image models. <https://github.com/rwightman/pytorch-image-models>, 2019.
- Yuksekgonul, M., Zhang, L., Zou, J., and Guestrin, C. Beyond confidence: Reliable models should also consider atypicality. *arXiv preprint arXiv:2305.18262*, 2023.
- Yurtsever, E., Lambert, J., Carballo, A., and Takeda, K. A survey of autonomous driving: Common practices and emerging technologies. *IEEE Access*, 8:58443–58469, 2020. doi: 10.1109/ACCESS.2020.2983149.
- Zadrozny, B. and Elkan, C. Learning and making decisions when costs and probabilities are both unknown. In *Proceedings of the Seventh ACM SIGKDD International Conference on Knowledge Discovery and Data Mining, KDD '01*, pp. 204–213, New York, NY, USA, 2001. Association for Computing Machinery. ISBN 158113391X. doi: 10.1145/502512.502540. URL <https://doi.org/10.1145/502512.502540>.
- Zadrozny, B. and Elkan, C. Transforming classifier scores into accurate multiclass probability estimates. In *Proceedings of the Eighth ACM SIGKDD International Conference on Knowledge Discovery and Data Mining, KDD '02*, pp. 694–699, New York, NY, USA, 2002. Association for Computing Machinery. ISBN 158113567X. doi: 10.1145/775047.775151. URL <https://doi.org/10.1145/775047.775151>.
- Zagoruyko, S. and Komodakis, N. Wide residual networks. In *BMVC*, 2016.
- Zhang, J., Kailkhura, B., and Han, T. Mix-n-match: Ensemble and compositional methods for uncertainty calibration in deep learning. In *International Conference on Machine Learning (ICML)*, 2020.

Table 2. (Extended Experiment on Tab. 1) Main results displaying changes after TNA, in accuracy and calibration performance. The experiments were conducted SVHN dataset expanded on the main result in Tab. 1, evaluating four different model architectures for each dataset. In addition to applying five recalibration techniques, including the uncalibrated model as a baseline, we evaluate TNA(sparse) and TNA(comp.), which involve two stages of optimization and explore the entire search space, respectively. In a specific dataset-model combination, indicate the technique that achieved the best results among all methods in **bold**, and underline the technique that achieved the best results without using proposed method. The results are displayed as averages over five runs.

	SVHN-WideResNet28x10			SVHN-MobileNetV2			SVHN-PreResNet110			SVHN-GoogleNet		
Methods	Acc. (\uparrow)	ECE (\downarrow)	AdaECE (\downarrow)	Acc. (\uparrow)	ECE (\downarrow)	AdaECE (\downarrow)	Acc. (\uparrow)	ECE (\downarrow)	AdaECE (\downarrow)	Acc. (\uparrow)	ECE (\downarrow)	AdaECE (\downarrow)
None	97.02 _{.06}	1.86 _{.04}	1.82 _{.04}	95.74 _{.03}	0.54 _{.02}	0.52 _{.02}	96.61 _{.03}	1.58 _{.03}	1.58 _{.03}	96.3 _{.06}	2.31 _{.04}	2.3 _{.04}
+TNA	97.0 _{.06}	0.45 _{.01}	0.49 _{.02}	95.75 _{.03}	0.43 _{.02}	0.45 _{.03}	96.56 _{.03}	0.53 _{.07}	0.74 _{.04}	96.29 _{.06}	0.59 _{.03}	0.99 _{.04}
IROvA	96.97 _{.06}	0.65 _{.18}	0.44 _{.03}	95.77 _{.06}	0.87 _{.17}	0.5 _{.14}	96.64 _{.08}	0.76 _{.15}	0.53 _{.12}	96.25 _{.1}	0.66 _{.18}	0.74 _{.1}
+TNA(sparse)	96.96 _{.07}	0.55 _{.22}	0.42 _{.06}	95.77 _{.06}	0.84 _{.19}	0.46 _{.1}	96.59 _{.08}	0.72 _{.16}	0.51 _{.14}	96.26 _{.08}	0.64 _{.18}	0.67 _{.11}
+TNA(comp.)	96.99 _{.04}	0.49 _{.15}	0.42 _{.11}	95.81 _{.05}	0.77 _{.17}	0.44 _{.1}	96.58 _{.06}	0.71 _{.22}	0.54 _{.09}	96.28 _{.03}	0.55 _{.01}	0.63 _{.04}
TS	97.02 _{.06}	0.67 _{.08}	0.55 _{.04}	95.74 _{.03}	0.33 _{.05}	0.28 _{.06}	96.61 _{.03}	0.76 _{.19}	0.87 _{.12}	96.3 _{.06}	1.01 _{.14}	1.07 _{.06}
+TNA(sparse)	97.0 _{.06}	0.61 _{.1}	0.5 _{.04}	95.75 _{.03}	0.32 _{.05}	0.25 _{.04}	96.56 _{.03}	0.64 _{.15}	0.83 _{.11}	96.29 _{.06}	0.97 _{.12}	1.01 _{.05}
+TNA(comp.)	97.01 _{.03}	0.44 _{.07}	0.44 _{.06}	95.75 _{.03}	0.32 _{.05}	0.25 _{.04}	96.5 _{.03}	0.53 _{.12}	0.68 _{.1}	96.29 _{.06}	0.97 _{.12}	1.01 _{.05}
ETS	97.02 _{.06}	0.67 _{.08}	0.55 _{.04}	95.74 _{.03}	0.34 _{.05}	0.28 _{.05}	96.61 _{.03}	0.76 _{.19}	0.87 _{.12}	96.3 _{.06}	1.01 _{.14}	1.07 _{.06}
+TNA(sparse)	97.0 _{.06}	0.61 _{.1}	0.5 _{.04}	95.75 _{.03}	0.33 _{.05}	0.25 _{.04}	96.56 _{.03}	0.65 _{.14}	0.84 _{.11}	96.29 _{.06}	0.97 _{.12}	1.01 _{.05}
+TNA(comp.)	97.01 _{.03}	0.44 _{.07}	0.44 _{.06}	95.79 _{.05}	0.32 _{.07}	0.25 _{.01}	96.49 _{.05}	0.52 _{.12}	0.68 _{.1}	96.29 _{.06}	0.97 _{.12}	1.01 _{.05}
AAR	97.04 _{.05}	0.32 _{.12}	0.29 _{.11}	95.83 _{.03}	0.35 _{.06}	0.3 _{.06}	96.66 _{.06}	0.51 _{.1}	0.48 _{.16}	96.32 _{.07}	0.43 _{.08}	0.43 _{.09}
+TNA(sparse)	97.03 _{.06}	0.3 _{.13}	0.28 _{.11}	95.84 _{.03}	0.34 _{.06}	0.3 _{.06}	96.65 _{.06}	0.49 _{.11}	0.47 _{.13}	96.31 _{.06}	0.4 _{.1}	0.42 _{.09}
+TNA(comp.)	97.0 _{.04}	0.3 _{.1}	0.29 _{.08}	95.88 _{.04}	0.27 _{.1}	0.29 _{.07}	96.62 _{.06}	0.41 _{.11}	0.38 _{.05}	96.31 _{.06}	0.4 _{.1}	0.42 _{.09}

A. Extended Experiments

A.1. (Extended Experiment on Tab. 1) Main Results on SVHN dataset.

The table reports the results for the SVHN dataset in Tab. 2. Similar trends to those shown in Tab. 1 are observed in this dataset as well.

A.2. (Extended Experiment on Fig. 4) Accuracy Compensation as increase of n_e across datasets and models.

In this section, to illustrate the ability to interpolate accuracy across different models, we conduct additional accuracy compensation experiments for two datasets, CIFAR10 (left column) and CIFAR100 (right column), considering three model architectures: WideResNet28x10 (upper), MobileNetV2 (middle), and PreResNet110 (lower). We increase the number n_e and observe the interpolation of accuracy. To assess how accuracy is interpolated on average, we utilize boxplots and statistically plot accuracy interpolation by repeating the presentation algorithm 10 times. The red dashed line represents the performance of the original weights, and the numerical values on the left indicate the quantification of accuracy changes. Negative values indicate a degradation in accuracy, and as observed in the Fig. 6, increasing n_e leads to better accuracy interpolation.

A.3. (Extended Experiment on Fig. 5) The shifting effect of angles across dataset and models.

To demonstrate that the proposed angle-shifting effect exists across all datasets and models, additional figures are presented as follows. Firstly, in Fig. 7, plots for combinations not included in the main paper are provided for wideResNet28x10, MobileNetV2, PreResNet110, and GoogleNet on CIFAR10 and CIFAR100 datasets. The plots showcase the shifting effect of angles across models and datasets.

B. Further Analysis, Ablation Studies

TNA : The optimization curve. We report the results of TNA after weight averaging is done when using 10 ensembles, $n_e = 10$ in Fig. 9. We utilize the calibration set to optimize the process and determine the best trained weights. It is important to note that the curve is unimodal a, and thus it is quite straight-forward to find the optimal angle of mRC , when TNA is applied.

Assumptions. In our study, various assumptions were made to demonstrate that the algorithm has confidence calibration effects. We reiterate some of the assumptions and provide deeper explanations. In detail, we elucidate the assumptions of 1) $\angle(\mathbf{w}_i, R\mathbf{w}_i)$ is equal across classes $i \in [C]$, and 2) the dimension n is high-dimensional in the appendix, Appendix B.

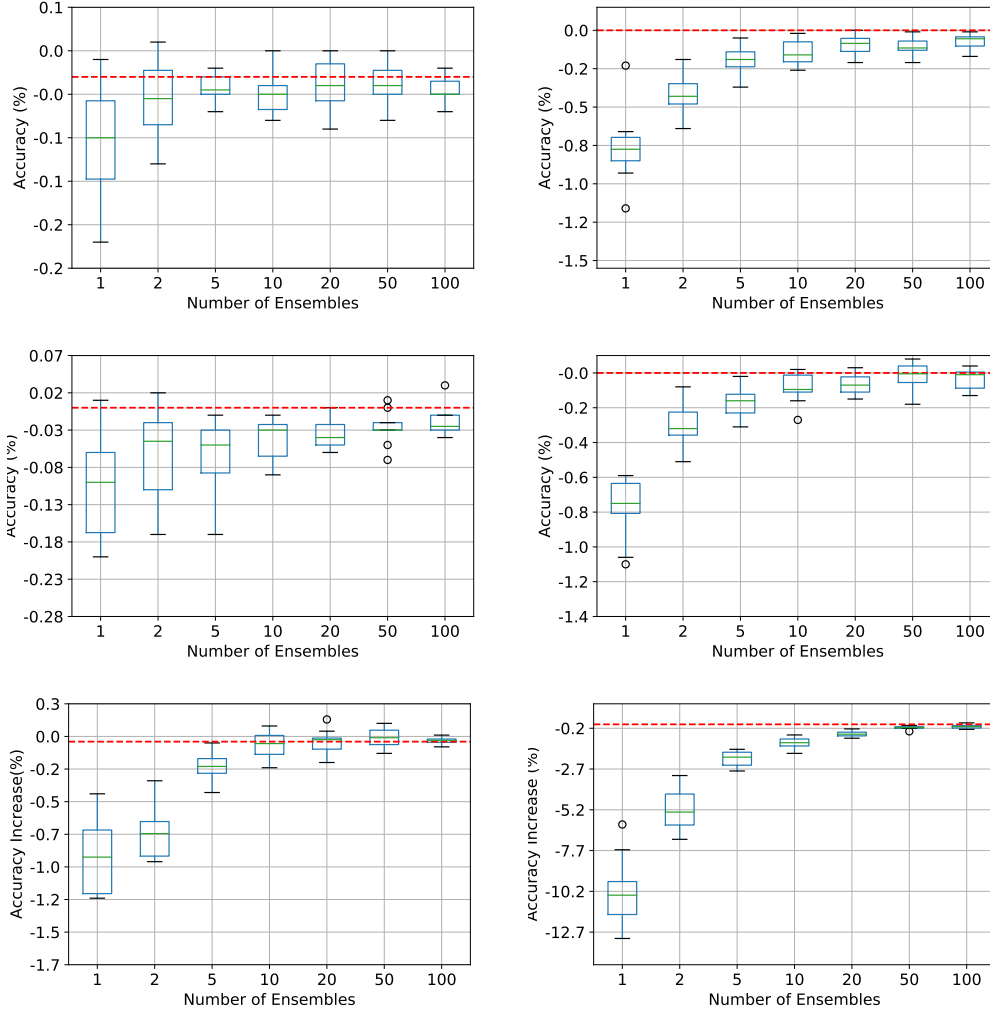


Figure 6. **Extended experiment on Fig. 4** on CIFARs. Plots of the accuracy of the ensembled outputs correspond to the number of ensemble members, on CIFAR10(left column) and CIFAR100(right column) dataset. The first row states the results on WideResNet28x10, middle row states the results on MobileNetV2, and the third row states the results on PreResNet110. The accuracy is well compensated as the n_e increases.

1) $\angle(\mathbf{w}_i, R\mathbf{w}_i)$ is equal across classes $i \in [C]$: $\angle(\mathbf{w}_i, R\mathbf{w}_i)$ might vary across classes. This situation arises when the rotation transform generated from the proposed algorithm TILT adjusts angles differently for each class. This violates the assumption in Prop. 3.3 which assumes $\forall i \in [C], \angle(\mathbf{w}_i, \mathbf{z}) = \theta$. Experimentally, as shown in Fig. 2, the left column describes the mean of rotation over classes, while the right column describes the standard deviation of rotation over classes. One observation is that in all cases, the standard deviation is not large, but it can occur when the number of classes C is small (i.e. CIFAR10, $C = 10$), number of rotations n_r is small, or θ_s is small. To address this issue and create a rotation corresponding to a specific $mRC(W, R) = \theta$, using a small value for θ_s and increasing the value of n_r can be effective.

2) The penultimate feature space is high-dimensional : The assumption $\Delta_{\mathbf{z}, i} = \arccos(\cos \psi_i \cos \theta) - \psi_i$ is associated with the high-dimensionality assumption. As mentioned in the "Blessings of the dimensionality" section in Section 5, the essence of our approach is to apply a transformation to the class vector based on intensity, adjusting the correlation with the penultimate feature. When a high-intensity transform is applied, the correlation between the penultimate feature and the class vector decreases, approaching 90 degrees, as indicated by the near orthogonal theorem. If the dimensionality decreases, the effectiveness of the algorithm may diminish. To verify this, we present additional ablation studies in Tab.3 and Fig.10. First, in Tab.3, we varied the dimension n of the last linear layer while training WideResNet28x10(Zagoruyko

& Komodakis, 2016), MobileNetV2(Sandler et al., 2018), and EfficientNetB0(Li & Vasconcelos, 2019) on CIFAR10 and CIFAR100 datasets. The additional linear layer is added in between the feature extractor and the final linear layer for the experiment. We measured the ECE, and it is evident that the effectiveness of the algorithm decreases as n decreases for both datasets. Next, in Fig.10, we measured the utility of the TILT algorithm as n decreases. The left figure, similar to Fig. 2, measures mRC by increasing n_r , and it shows that the narrower the n , the wider the range of mRC generated by a specific n_r . Therefore, it indicates the need for delicate adjustment of mRC for optimal performance of the proposed algorithm. The middle and right figures measure the decrease in accuracy for different mRCs in situations with a single tilted weight (middle) and TNA weight $n_e = 10$ (right). Again, it confirms that as n decreases, accuracy performance degradation occurs at smaller angles.

Table 3. Expected Calibration Error in percentage(%) for two datasets with respect to change in the number of dimension(n) in the penultimate feature(pf), CIFAR100 (left) and CIFAR10(right). None stands for unscaled, TNA (Tilt and Average), TS(Temperature Scaling), and TS+TNA. The number aside to the architecture, with the parentheses denote the original dimension. Bold for the best calibrated, underline for the second best. Lower the better.

Model	n	CIFAR100				CIFAR10			
		None	TNA	TS	+TNA	None	TNA	TS	+TNA
WRN28x10 (640)	10	11.05	11.04	<u>1.41</u>	1.40	1.73	1.48	0.7	0.48
	40	7.24	<u>2.21</u>	3.10	2.18	1.78	0.55	0.58	0.54
	160	7.25	<u>2.66</u>	2.84	2.05	2.20	0.60	0.83	0.54
	640	5.91	<u>4.11</u>	4.69	4.55	1.66	0.66	0.84	0.78
MNV2(1280)	20	10.23	10.23	<u>1.85</u>	1.80	3.44	2.78	<u>0.79</u>	0.65
	80	10.92	1.74	<u>1.48</u>	1.31	3.09	<u>0.58</u>	0.69	0.53
	320	11.51	<u>1.26</u>	1.52	1.19	3.51	<u>0.66</u>	0.68	0.54
	1280	10.03	<u>1.54</u>	1.82	1.41	3.49	0.78	1.06	<u>0.81</u>
EffB0(320)	40	10.9	1.63	<u>1.59</u>	1.37	2.74	1.15	<u>0.96</u>	0.86
	80	10.7	1.52	1.32	1.32	3.67	<u>0.85</u>	0.95	0.71
	160	10.23	<u>1.24</u>	1.29	1.01	3.24	<u>0.73</u>	0.81	0.66
	320	14.8	<u>1.56</u>	1.77	1.34	4.65	0.82	1.12	<u>0.95</u>

C. Proof of Theorem 3.2

Proof. For the purpose of descriptive convenience, let u be the direction vector of class vector w_i be u , and direction vector of penultimate vector z be v and ψ_i be ψ . Without loss of generality, let u be a unit vector pointing at the north pole of the first dimension. $u = [1, 0, \dots, 0]$, and $v = [v_1, v_2, \dots, v_n]$ Then the vector v lies in the space where $\angle(u, v) = \arccos(u \cdot v) = \psi$. That is,

$$u \cdot v = v_1 = \cos \psi, v_2^2 + \dots + v_n^2 = 1 - \cos^2 \psi = \sin^2 \psi. \quad (9)$$

Without loss of generality, we can also suppose that the plane u, v lies in the subspace spanned by two basis vectors $[1, 0, \dots, 0]$ and $[0, 1, 0, \dots, 0]$, which means $v_1 = \cos \psi, v_2 = \sin \psi, v_3 = v_4 = \dots = 0$.

The rotated vector of v , $R_\theta(v) = [t_1, t_2, \dots, t_n]$ will lie in the trace of the intersection of the surface of the n -dimension hypersphere where $t_1^2 + t_2^2 + \dots + t_n^2 = 1$ and $v \cdot R_\theta(v) = \cos \theta$. $t_1 \cos \psi + t_2 \sin \psi = \cos \theta$. As a function of t_1 , $\{t_2, t_3, \dots, t_n\}$ has the trace of,

$$\begin{aligned} t_2 &= \frac{\cos \theta - t_1 \cos \psi}{\sin \psi}, \\ t_3^2 + t_4^2 + \dots + t_n^2 &= 1 - t_1^2 - t_2^2 \\ &= 1 - t_1^2 - \left(\frac{\cos \theta - t_1 \cos \psi}{\sin \psi} \right)^2, \end{aligned} \quad (10)$$

that is when t_1 is fixed, $\{t_3, \dots, t_n\}$ will lie in the surface of the $n - 2$ dimensional hypersphere of radius

$$\sqrt{1 - t_1^2 - \left(\frac{\cos \theta - t_1 \cos \psi}{\sin \psi} \right)^2}.$$

$$\begin{aligned}
 & 1 - t_1^2 - \left(\frac{\cos \theta - t_1 \cos \psi}{\sin \psi} \right)^2 \\
 &= 1 - t_1^2 - \frac{\cos^2 \theta - 2t_1 \cos \psi \cos \theta + t_1^2 \cos^2 \psi}{\sin^2 \psi} \\
 &= -\frac{1}{\sin^2 \psi} t_1^2 + \frac{2 \cos \psi \cos \theta}{\sin^2 \psi} t_1 - \frac{\cos^2 \theta}{\sin^2 \psi} + 1 \\
 &= -\frac{1}{\sin^2 \psi} (t_1^2 - 2 \cos \psi \cos \theta t_1 + \cos^2 \psi \cos^2 \theta) \\
 &\quad + \frac{\cos^2 \psi \cos^2 \theta}{\sin^2 \psi} - \frac{\cos^2 \theta}{\sin^2 \psi} + \frac{\sin^2 \psi}{\sin^2 \psi} \\
 &= -\frac{1}{\sin^2 \psi} (t_1 - \cos \psi \cos \theta)^2 + \sin^2 \theta,
 \end{aligned} \tag{11}$$

and yields its maximum value when $t_1 = \cos \psi \cos \theta$. Also

$$\begin{aligned}
 t_3^2 + t_4^2 + \dots + t_n^2 &= 1 - t_1^2 - t_2^2 \\
 &= -\frac{1}{\sin^2 \psi} (t_1 - \cos \psi \cos \theta)^2 + \sin^2 \theta \geq 0
 \end{aligned} \tag{12}$$

gives the fact that $\cos(\psi + \theta) \leq t_1 \leq \cos(\psi - \theta)$, because the quadratic function is unimodal. The angle $\angle(u, R_\theta(v)) = \arccos u \cdot v = \arccos t_1$ is a strictly decreasing function, to find the mode it is sufficient to find the t_1 ,

$$\mathbb{M}[\Delta] = \arccos \left(\arg \max_{t_1} \sqrt{1 - t_1^2 - \left(\frac{\cos \theta - t_1 \cos \psi}{\sin \psi} \right)^2} \right) - \psi, \tag{13}$$

which is proved to yield its maximum value when $t_1 = \cos \psi \cos \theta$.

Additionally,

$$\begin{aligned}
 & \frac{\partial}{\partial \psi} (\arccos(\cos \psi \cos \theta) - \psi) \\
 &= -\frac{1}{\sqrt{1 - (\cos \psi \cos \theta)^2}} \cdot (-\sin \psi) \cdot (\cos \theta) - 1 \\
 &= \frac{\sin \psi \cos \theta}{\sqrt{1 - \cos^2 \psi \cos^2 \theta}} - 1 \\
 &< \frac{\sin \psi}{\sqrt{1 - \cos^2 \psi}} - 1 = \frac{\sin \psi}{\sin \psi} - 1 = 0,
 \end{aligned} \tag{14}$$

and the $\mathbb{M}[\Delta_{z,i}] = \arccos(\cos \psi \cos \theta) - \psi$ is the strictly decreasing function of ψ .

□

D. Real-life Implications

(Pneumonia Diagnosis Case.) First, consider a binary classification problem, specifically diagnosing pneumonia using only chest images (Daniel Kermany, 2018)(a), (b), (c)). In case (a), where the individual is diagnosed with pneumonia, the confidence in pneumonia infection exceeds 0.9, indicating a high confidence level in the correct prediction. However, in case (b), a high confidence of 0.98 was assigned to the prediction of not having pneumonia. After calibration, the confidence level decreases to 0.62. This lower confidence level in binary classification may serve as a signal of uncertainty in the decision. False negatives and false positives can be life-threatening in the medical domain.

(Egg Classification Case.) Consider the task of discerning fresh eggs (Hub, 2022)(d),(e),(f). This task involves classifying eggs based on their photos into different categories such as Normal, Cracked Egg, Deformed Egg, and Dirty Egg. We may utilize the confidence of the calibrated model as an indicator of uncertainty (e.g., using a threshold of 0.5). In case (d), an

egg with a crack is correctly classified as a cracked egg after calibration with high confidence. In case (e), where a saleable egg is misclassified as a Deformed Egg with miscalibrated high confidence, and can be discarded. In case (f), a cracked egg can be misclassified as a dirty egg, where some of the dirty eggs can be sold after washing, but eggs with cracks cannot be sold after washing . This could lead to significant losses for the farm.

E. Experimental Details

	lr_{init}	epochs	wd	batch size
WideResNet28x10	0.1	300	5e-4	128
GoogleNet	0.1	300	5e-4	128
MobileNetV2	0.1	250	3e-4	128
PreResNet110	0.1	300	5e-4	128

Table 4. Training Details of trained weights for SVHN.

	lr_{init}	epochs	wd	batch size
WideResNet28x10	0.1	300	5e-4	128
GoogleNet	0.1	300	3e-4	128
MobileNetV2	0.01	250	3e-4	128
PreResNet110	0.1	300	3e-4	128

Table 5. Training Details of trained weights for CIFAR10 and CIFAR100.

We list the detailed information to conduct the experiments that are included in the main paper.

Model Family. The alternative weights are generated on WideResNet28x10(Zagoruyko & Komodakis, 2016), GoogleNet(Szegedy et al., 2015), PreResNet110(He et al., 2016a), and MobileNetV2(Sandler et al., 2018) for CIFARs, and ResNet-50(He et al., 2016a), and DenseNet169(Huang et al., 2017), ViT-L/16, and ViT-H/14(Dosovitskiy et al., 2021) . To train the model for the CIFAR10, and CIFAR100, we followed the standard training scheme and evaluation code borrowed from the pioneering work of (Ashukha et al., 2020), with the training information written in Tab. 4, 5 , and 6. For the ImageNet-1k dataset, the trained weights are borrowed from Timm(Wightman, 2019) and Torchvision (Marcel & Rodriguez, 2010). We fix the number of ensembles $n_e = 10$ for all the models.

Training Details. Most of the settings to train SVHN/CIFAR10/CIFAR100 networks are taken from (Ashukha et al., 2020). Specifically, we used Momentum-SGD with batch size of 128, momentum 0.9. The batch size is fixed to 256. The learning rate scheduler follows the work of (Garipov et al., 2018) and is specified as,

$$lr(i) \equiv \begin{cases} lr_{init} & \frac{i}{epochs} \in [0, 0.5] \\ lr_{init}(1.0 - 0.99(\frac{i}{epochs} - 0.5)) & \frac{i}{epochs} \in [0.5, 0.9] \\ lr_{init} \times 0.01 & otherwise \end{cases} \quad (15)$$

The information of the trained models is listed in Table. 7.

	Acc. (SVHN)	Acc. (CF10)	Acc. (CF100)	Image Size	Interpolation	Mean	Std
WideResNet28x10	97.03	96.42	81.25	32	padding=4	[0.4914, 0.4822, 0.4465]	[0.2023, 0.1994, 0.2010]
GoogleNet	96.32	95.24	79.41	32	padding=4	[0.4914, 0.4822, 0.4465]	[0.2023, 0.1994, 0.2010]
MobileNetV2	95.64	92.58	73.41	32	padding=4	[0.4914, 0.4822, 0.4465]	[0.2023, 0.1994, 0.2010]
PreResNet110	96.565	94.71	77.74	32	padding=4	[0.4914, 0.4822, 0.4465]	[0.2023, 0.1994, 0.2010]

Table 6. The information of the trained models for CIFAR10 and CIFAR100 datasets. We list the top-1, top-5 accuracy, and train / test transformations for the images.

Hyperparameters. Generally we set the number of ensembles $n_e = 10$ for all the results, and $\alpha = 5, \beta = 1$ for the hyperparameters for beta distribution. θ_s is set to 0.9rad if not stated. The search interval of rotation number n_t is set to

Tilt and Average : Geometric Adjustment of the Last Layer for Recalibration

	Top-1	Top-5	Image Size	Crop Percentage	Interpolation	Mean	Std
ResNet-50	76.11	92.862	224	0.875	bicubic	[0.485, 0.456, 0.406]	[0.229, 0.224, 0.225]
DenseNet-169	75.6	92.806	224	0.875	bicubic	[0.485, 0.456, 0.406]	[0.229, 0.224, 0.225]
ViT-L/16	84.24	97.818	224	0.9	bicubic	[0.485, 0.456, 0.406]	[0.229, 0.224, 0.225]
ViT-H/14	85.708	97.73	224	0.875	bicubic	[0.485, 0.456, 0.406]	[0.229, 0.224, 0.225]

Table 7. The information of the trained models for ImageNet datasets. We list the top-1, top-5 accuracy, and train / test transformations for the images.

50. We set three different θ_s for all the models, of 0.5, 1.0, 1.5 . The value of θ_s for Fig. 2 is specified in the figure. n , the dimension of the penultimate feature(pf), is a pre-determined value from the model, with values corresponding to each model.

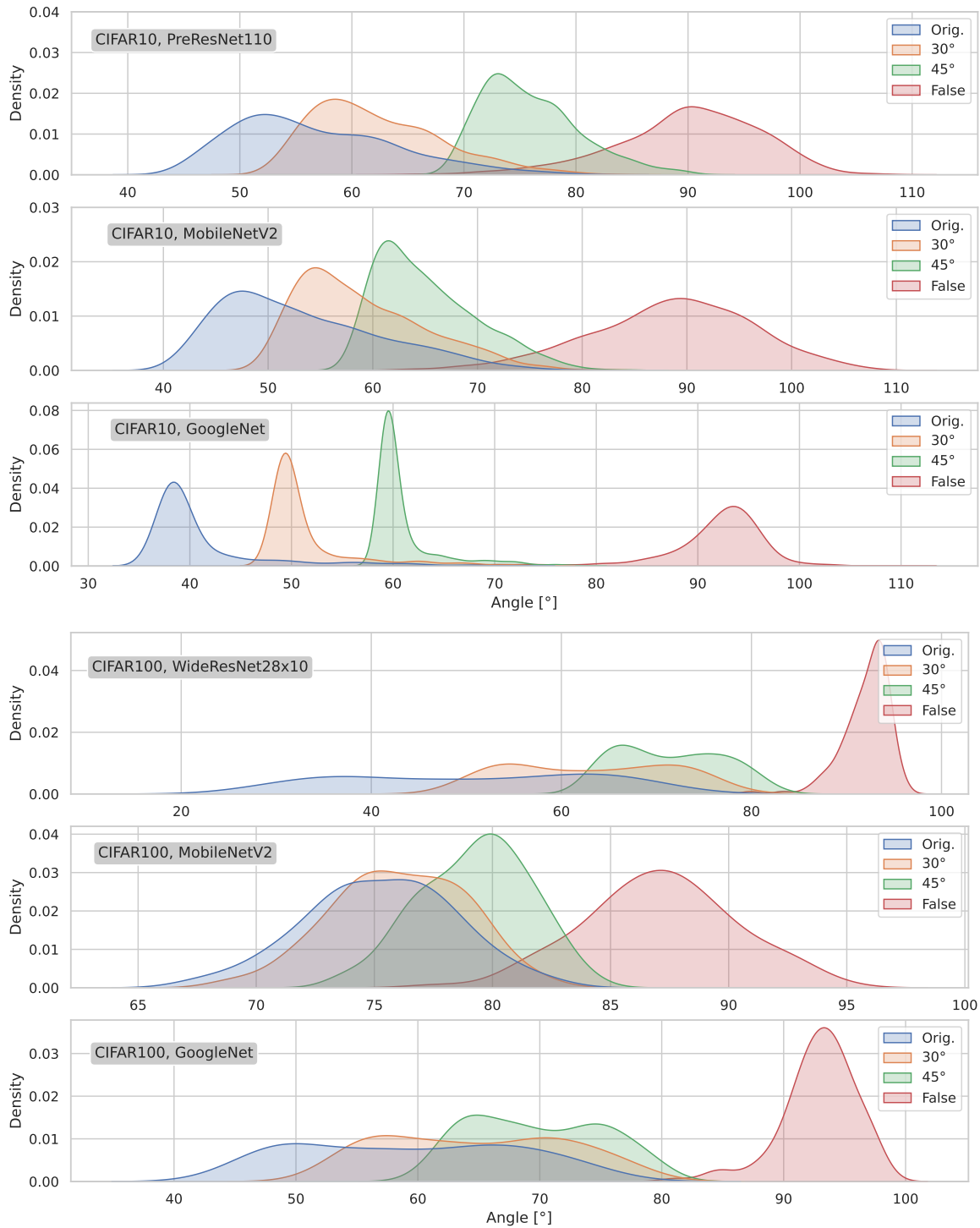


Figure 7. **Extended experiment on Fig. 3** on CIFARs. Distribution plot of the data samples with angle between class vector and pf , $\angle(\mathbf{w}_i, \mathbf{z}_x)$, with the corresponding predicted class row vector of the **original weight** (Orig.) and the **tilted weights** by depicted angle of mRC (30° , 45°). “False” denotes the angle of pf with the class vector does not correspond to the respective class. As the mRC increases, the angles shift towards 90° . Best seen with colors.

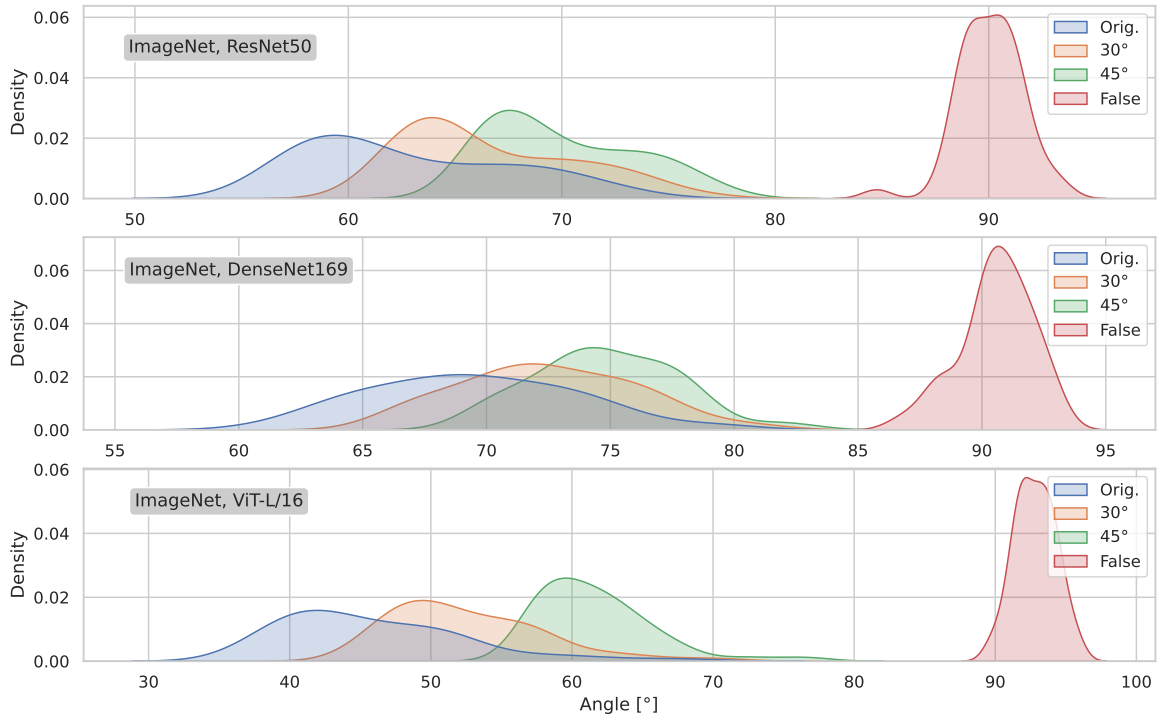


Figure 8. Extended experiment on Fig. 3 on ImageNet dataset. Distribution plot of the data samples with angle between class vector and pf , $\angle(\mathbf{w}_i, \mathbf{z}_x)$, with the corresponding predicted class row vector of the **original weight** (Orig.) and the **tilted weights** by depicted angle of mRC (30°, 45°). “False” denotes the angle of pf with the class vector does not correspond to the respective class. As the mRC increases, the angles shift towards 90°. Best seen with colors.

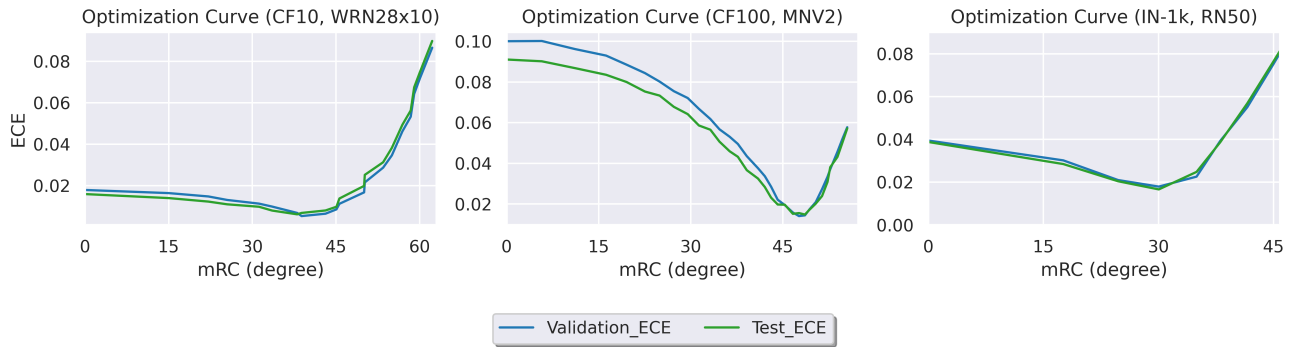


Figure 9. The optimization curve when TNA is done with number of ensembles $n_e = 10$. We leverage the calibration set to optimize and find the optimal trained weights, applying grid search with the calibration dataset’s information allowed (‘Validation_ECE’). The ‘Test_ECE’, ECE on the test dataset, exhibits similar trend with the ‘Validation_ECE’. Note that the curve is unimodal, making it able to optimize.

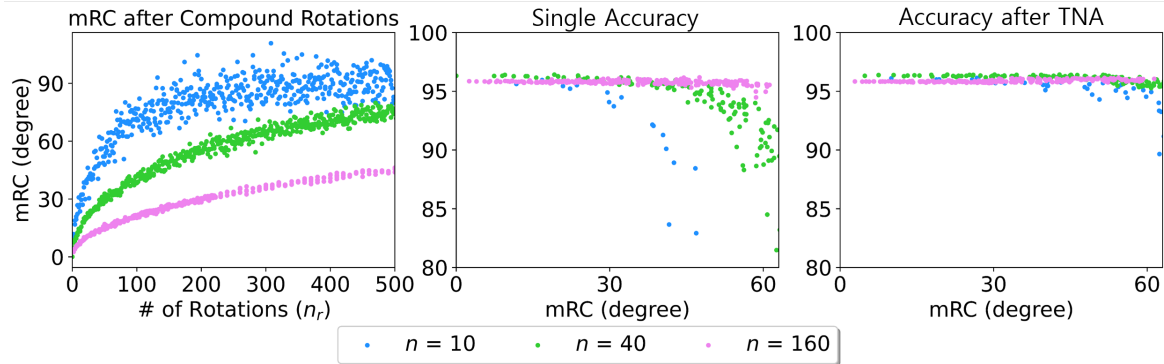


Figure 10. Ablation study of when the dimension of penultimate feature n decrease. The experiment is done on CIFAR-10 dataset, with WideResNet28x10. Here when n is set to lower values, the mRC tend to have larger deviation for a certain n_r , making it harder for the user to generate for a certain mRC. Thus the accuracy interpolation performance degrades after TNA.

Domain, Task	Medical, Pneumonia Diagnosis			Farming, Egg Classification		
Image Example						
	(a)	(b)	(c)	(d)	(e)	(f)
Ground Truth	Pneumonia	Pneumonia	Normal	Cracked Egg	Normal	Cracked Egg
Prediction, Confidence (Uncalibrated)	Pneumonia 0.999	Normal 0.98	Pneumonia 0.98	Cracked Egg 0.994	Deformed Egg 0.986	Dirty Egg 0.984
Prediction, Confidence (TNA Calibrated)	Pneumonia 0.964	Normal 0.62	Pneumonia 0.67	Cracked Egg 0.981	Deformed Egg 0.424	Dirty Egg 0.57

Figure 11. Real-life examples of confidence calibration.